



ELSEVIER

Contents lists available at ScienceDirect

Continental Shelf Research

journal homepage: www.elsevier.com/locate/csr

Research papers

The contribution of short-waves in storm surges: Two case studies in the Bay of Biscay

Xavier Bertin^{a,*}, Kai Li^a, Aron Roland^b, Jean-Raymond Bidlot^c^a UMR 7266 LIENSs CNRS-Université de La Rochelle, Institut du Littoral et de l'Environnement, 2 rue Olympe de Gouges, 17000 La Rochelle, France^b BGS IT&E GmbH, D-64297 Darmstadt, Pfungstaedter Strasse 37, Germany^c European Centre for Medium Range Weather Forecasts, Reading, United Kingdom

ARTICLE INFO

Article history:

Received 31 January 2014

Received in revised form

17 December 2014

Accepted 6 January 2015

Available online 14 January 2015

Keywords:

Storm surge

Unstructured grid

Surface stress

Wave setup

Friction velocity

Xynthia

Joachim

ABSTRACT

This study investigates the contributions of short waves in storm surges through the hindcast of two storms that hit the central part of the Bay of Biscay recently. Despite displaying comparable wind speed and directions in the study area, these two storms induced different storm surges and sea states. Xynthia (27–28th of February 2010) was characterized by large (up to 7 m significant wave height H_s) and short-period waves and induced an exceptional storm surge, locally larger than 1.6 m. The second storm, Joachim (15–16th of December 2011), was characterized by very large (up to $H_s > 10$ m) and long-period waves but only induced a storm surge almost two times lower. To investigate these differences, a new unstructured grid and fully coupled modeling system is applied, with a spatial resolution fine-enough to adequately represent the surf zones over most of the study area (25 m). The analysis of the modeling results and the available field observations reveals firstly that the exceptional surge during Xynthia originated from young and steep waves, enhancing surface stress. This particular sea-state is explained by the abnormal track of Xynthia, which restricted the fetch to a few hundred km. The wave radiation stress gradient locally induced setup larger than 0.4 m along the coastlines fully exposed to ocean waves, while wave setup in the range 0.1–0.2 m was also shown to develop regionally and to propagate in sheltered harbors. Comparatively, wave-enhanced bottom stress appears to be a second-order process and has a more limited impact on storm surges.

© 2015 Elsevier Ltd. All rights reserved.

1. Introduction

Tropical cyclones and extra-tropical storms making landfall in coastal zones are among the most costly natural disasters (Smith, 1996; Nicholls et al., 2007). Historically, the main part of the material and human losses in coastal zones is associated with coastal flooding rather than direct wind effects (Zhang et al., 2008). Coastal flooding predominantly occurs in low-lying zones under the concomitance of a large storm surge and a high spring tide, although the importance of this concomitance also depends on the ratio between the storm surge and the local tidal range. For instance, the more than 8 m storm surge induced by hurricane Katrina in 2005 (Blake, 2007) would have induced a major flooding in the microtidal coastlines of Louisiana, whatever the tidal phase might have been. The major catastrophes that occurred over the last decade, such as Katrina in the Gulf of Mexico (2005), Nargis in the Bay of Bengal (2008), Sandy in the New York area (2012) and

Haiyan in the Philippines (2013) remind us of the necessity of being able to predict storm surges accurately, although the physical processes controlling these phenomena remain only partly understood.

The effects of atmospheric pressure gradients and winds on sea-level were recognized early (e.g. Doodson, 1924) and were integrated in pioneer modeling approaches (e.g. Jelesnianski, 1965). Following these early quantitative approaches, many studies have shown that the wind-induced surface stress was the dominant process at coastal zones bordered by large and shallow shelves (Flather, 2001; Rego and Li, 2010; Kennedy et al., 2012). Tide–surge interactions were also shown early to be significant at some locations (e.g. Proudman, 1957; Rego and Li, 2010; Idier et al., 2012). By contrast, the contribution of short-waves in storm surges has only been investigated more recently. Thus, for a long time, it has been common practice to compute the wind surface stress based on bulk formula (Eq. (1)):

$$\tau_s = \rho_a C_d U_{10}^2 \quad (1)$$

where ρ_a is the air density, U_{10} is the 10 m wind speed and C_d is a drag coefficient corresponding to the sea roughness that increases

* Corresponding author. Fax: +33 546458274.

E-mail address: xbertin@univ-lr.fr (X. Bertin).

linearly with the wind speed for low to moderate winds (e.g. Smith and Banke, 1975; Pond and Pickard, 1998). However, based on the pioneer work of Charnock (1955), Stewart (1974) proposed that the sea roughness should also depend on the wave age for a given wind speed. The dependence of the surface stress on the sea state was then corroborated in many studies (Donelan et al., 1993; Mastenbroek et al., 1993; Brown and Wolf, 2009; Sheng et al., 2010; Olabarrieta et al., 2012). More recently, field measurements under extreme winds showed that the sea roughness could reach a maximum or even decrease due to wave-induced streaks of foam and sprays for winds larger than 35–40 m/s (Powell et al., 2003; Takagaki et al., 2012; Holthuijsen et al., 2012). In shallow water, orbital motions associated with short-wave propagation can also enhance bottom stress, thereby usually reducing storm surges (e.g. Nicolle et al., 2009). Nevertheless, the impact of this phenomenon on the surge peak is often found to be limited (Xie et al., 2003) while storm surge predictions are not always clearly improved when accounting for this process (e.g., Jones and Davies, 1998). In the nearshore, wave dissipation induces gradients of radiation stress (Longuet-Higgins and Stewart, 1964) that drive a setup easily reaching several tens of centimeter during storms. However, the proper representation of this phenomenon requires employing a very fine spatial resolution (e.g. of the order of 10 m), which poses a serious computational challenge when simulating storm surges at regional scale. This difficulty probably explains why only a limited number of studies have successfully accounted for wave setup at regional scale (e.g. Dietrich et al., 2010).

This study investigates the contribution of short waves in storm surges based on the hindcast of two extra-tropical storms that recently hit the central part of the Bay of Biscay (France): Xynthia on the 27–28th of February 2010 and Joachim on the 15–16th of December 2011. This study builds on a preliminary hindcast of the storm surge associated with Xynthia, which used an offline coupling between a circulation model and a spectral wave model and a coarse spatial resolution that prevented the representation of nearshore wave-induced processes (Bertin et al., 2012). Although both storms displayed comparable wind speed and directions over the study area, they induced different storm surges and sea states. The main purpose of this paper is to take advantage of these

contrasting case studies to investigate the contribution of short waves in storm surges. The section following this introduction describes the data and the fully coupled modeling system used in this study. Section 3 describes the studied area and both storms. The next section presents the modeling results in terms of atmospheric forcing, sea states and storm surges. Section 5 discusses the contribution of the three main wave-induced processes in storm surges: wave-enhanced surface and bottom stress and the gradients of radiation stress. Finally, the main findings of this study are summarized and some perspectives are given in the conclusion.

2. Methods and data

2.1. The storm surge modeling system

2.1.1. General overview

In this study, we applied the numerical modeling system Semi-implicit Eulerian–Lagrangian Finite Element (SELFE; Zhang and Baptista, 2008; Zhang et al., 2011), which now includes modules to simulate water quality (Rodrigues et al., 2011), oil spills (Azevedo et al., 2014) and sediment transport (Pinto et al., 2012). Recently, a full coupling was undertaken with the spectral wave model Wind Wave Model II (hereafter WWMII, Roland et al., 2012). The two codes share the same unstructured grid and the same domain decomposition, which makes this modeling system very computationally efficient and allows for massive parallel techniques. More details regarding coupling can be found in Roland et al. (2012). The unstructured grid used in this study employs 201,701 nodes (385,980 elements) and its resolution ranges from 30,000 m in the deep Ocean and far from the study area to 25 m along the shoreline of the study area (Fig. 1). Such a fine resolution together with the coupling strategy allow for a proper representation of nearshore wave-induced processes, which constitutes a major improvement compared to the preliminary hindcast of Xynthia described in Bertin et al. (2012). The computational grid is bounded by the shoreline, which means that the coastal areas flooded during Xynthia are not represented. Bertin et al. (2014) conducted

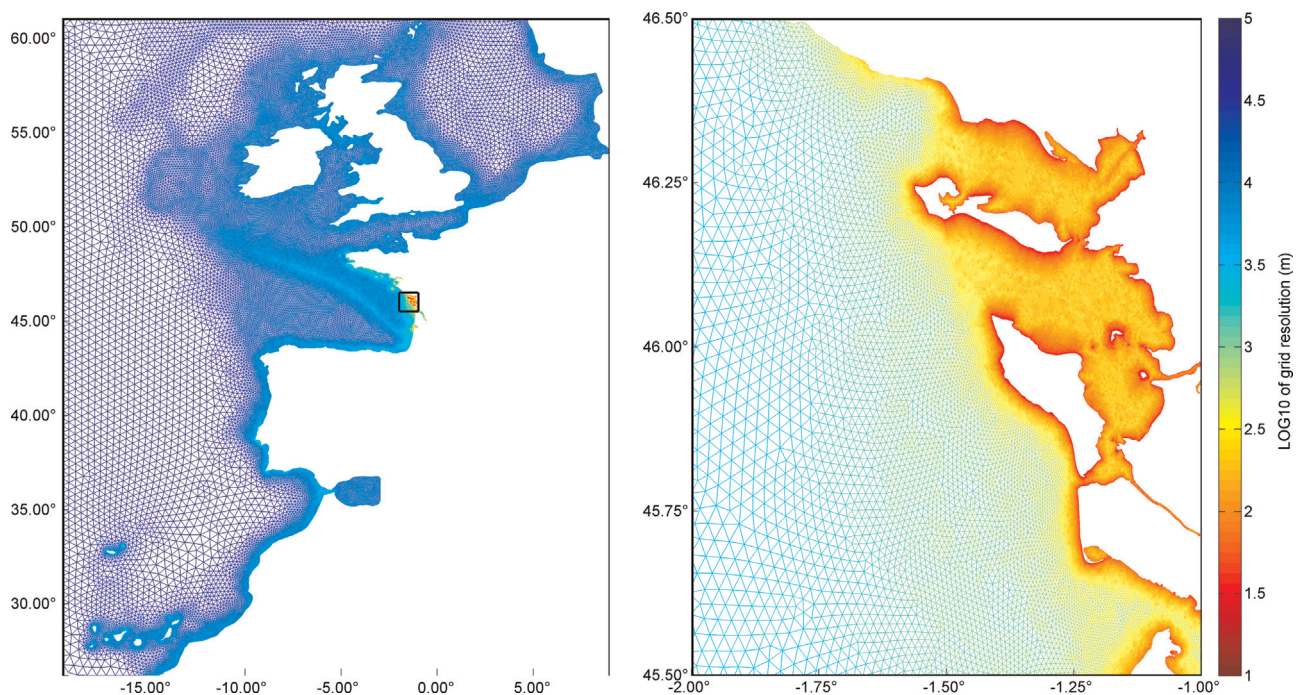


Fig. 1. Unstructured grid used in this study, showing a resolution ranging from 30,000 to 25 m.

a specific study on the flooding associated with Xynthia and showed that the massive flooding that occurred impacted water levels in estuaries significantly. However, these authors also showed that this effect was negligible at the tide gauges used in the present study (i.e. < 0.05 m). Finally, a time step of 60 s was selected for both models.

2.1.2. The spectral wave model

WWMII solves the wave action equation (Eq. (2)) on unstructured grid:

$$\frac{\partial N}{\partial t} + \frac{\partial(C_{gx} + U)N}{\partial x} + \frac{\partial(C_{gy} + V)N}{\partial y} + \frac{\partial(C_\sigma N)}{\partial \sigma} + \frac{\partial(C_\theta N)}{\partial \theta} = \frac{S_{tot}}{\sigma} \quad (2)$$

In this equation, N is the wave action, C_{gx} and C_{gy} are the x and y -components of the wave group velocity, U and V are the two horizontal components of the current velocity, σ and θ are the wave relative angular frequency and the wave direction and S corresponds to the sum of the source terms. Source terms include non-linear interactions, wind growth and dissipation by white-capping, bottom friction and wave breaking, which are computed according to the approaches JONSWAP (Hasselmann et al., 1973) and Battjes and Janssen (1978), respectively. Nonlinear 4-wave interactions are computed using the Discrete Interaction Approximation of Hasselmann et al (1985), and the Lumped Lumped Triad Approximation of Eldeberky (1996) in shallow water. Among these source terms, the wind input $S_{(\sigma,\theta)in}$ is of key importance in this study since the coupling with the circulation model is made through the friction velocity computed from the wave model. The approach used here is based on the quasi-linear theory of wave–atmosphere interactions and follows the pioneering work of Phillips (1957) and Miles (1957), later improved by Janssen (1989, 1991). This kind of approach is the one that is used in many operational wave forecasting systems worldwide (Bidlot et al., 2007a; Tolman, 2009) and on top of which further improvement could be made, e.g. Ardhuin et al. (2010). The formulation of the wind input source terms in the framework of the Wave Action Equation is given as follows:

$$S_{(\sigma,\theta)in} = \sigma \frac{\rho_a}{\rho_w \kappa^2} e^{ZZ^4} \left(\frac{U_*}{C} \right)^2 \max(\cos(\theta - \varphi), 0)^2 N_{(\sigma,\theta)} \quad (3)$$

where σ is the relative wave frequency ρ_a and ρ_w the air and water densities, respectively. κ is the von Karman constant and β_{max} is a non-dimensional growth parameter set to 1.22. C is the phase velocity, φ the wind direction at 10 m height and θ the discrete wave direction of the considered wave packet. Z is a function illustrating that the growth rate depends on the roughness length Z_0 , which inherently depends on the sea state:

$$Z = \ln \left(\frac{gZ_0}{C^2} \right) + \frac{\kappa}{\cos(\theta - \varphi)((U_*/C) + Z_\alpha)} \quad (4)$$

where z_α is a wave age tuning parameter set to 0.011. The roughness Z_0 is defined as

$$U_{10} = \frac{U_*}{\kappa} \ln \left(\frac{Z_{obs}}{Z_0} \right) \quad (5)$$

$$Z_0 = \frac{\alpha_0 U_*^2}{\sqrt{1 - (\tau_w/\tau)}} \quad (6)$$

where α_0 is a minimum value for the Charnock coefficient, Z_{obs} is the height at which the wind is taken (10 m), $\tau = U_*^2$ and τ_w is the wave supported stress, an integral function of the wind input source term. Therefore, Eqs. (5) and (6) provide an implicit functional dependence of U_* , U_{10} and τ_w/τ . Further details on

the parameterization of these source terms can be found in Bidlot et al. (2007b) and Bidlot (2012). An important consequence for this study is that this parameterization is very sensitive to the wave age C/U_* and to the roughness length Z_0 . A high-energy level in the high-frequency part of the spectrum will lead to larger values for Z_0 and U_* , which will result in a positive feedback and reinforce the energy levels.

In this version of the code, we have adopted to our best knowledge the parameterization described in Bidlot et al. (2007b). However, this does not correspond exactly to the latest developments carried out at the European Center for Medium range Weather Forecast (hereafter ECMWF), which include for example modifications for shallow waters. Another limitation of our approach is that we employed the total air-side stress to force our circulation model while it should be corrected from the amount of momentum absorbed and released by the wave field (Janssen et al. 2004, 2013). The impact of this limitation as well as the latest development carried at ECMWF for shallow waters will have to be investigated in future studies.

A four-step fractional method is employed, according to Yanenko (1971). First, advection in geographic space is solved using the explicit N-Scheme (e.g. Abgrall, 2006). Advection in spectral space is then solved using the Ultimate Quickest finite difference scheme of Leonard (1991) as done in WaveWatchIII (hereafter WWIII; Tolman, 2009). Finally, the source terms S are integrated in a similar manner as in WWIII. WWMII is forced by wind fields originating from series of 12 h forecasts from the operational high resolution model of ECMWF (0.125°/1 h) over the whole domain. Along the open boundary, WWMII is forced with time-series of spectra computed from a regional application of WWIII for the North Atlantic Ocean described in Dodet et al. (2010) and Bertin et al. (2013). Fields of currents and water levels are provided by SELFE at each hydrodynamic time step (60 s) while WWMII provides SELFE with fields of wave radiation stress, friction velocities as well as wave directions and orbital bottom velocities used to compute bottom stress.

2.1.3. The circulation model

The horizontal circulation is computed with SELFE (Zhang and Baptista, 2008), which solves the full Navier Stokes equation over unstructured grids and was designed to address a large range of spatio-temporal scales. In this study, SELFE is used in 2DH barotropic mode and the resolved equations are the following (Eqs. (7)–(9)):

$$\frac{\partial \zeta}{\partial t} + \vec{\nabla} \cdot \int_{-h}^{\zeta} \vec{u} dz = 0 \quad (7)$$

$$\begin{aligned} \frac{DU}{Dt} = fV + \alpha g \frac{\partial \hat{\psi}}{\partial x} - \frac{1}{\rho_w} \frac{\partial P_A}{\partial x} - g \frac{\partial \zeta}{\partial x} + \frac{\tau_{sx} - \tau_{bx}}{\rho_w(\zeta + h)} \\ - \frac{1}{\rho_w(\zeta + h)} \left(\frac{\partial S_{xx}}{\partial x} + \frac{\partial S_{xy}}{\partial y} \right) \end{aligned} \quad (8)$$

$$\begin{aligned} \frac{DV}{Dt} = -fU + \alpha g \frac{\partial \hat{\psi}}{\partial y} - \frac{1}{\rho_w} \frac{\partial P_A}{\partial y} - g \frac{\partial \zeta}{\partial y} + \frac{\tau_{sy} - \tau_{by}}{\rho_w(\zeta + h)} \\ - \frac{1}{\rho_w(\zeta + h)} \left(\frac{\partial S_{yy}}{\partial y} + \frac{\partial S_{xy}}{\partial x} \right) \end{aligned} \quad (9)$$

where ζ is the free surface elevation, h is the bathymetry, ρ_w is the water density, g is the acceleration due to gravity, f is the Coriolis parameter, P_A is the sea-level atmospheric pressure, and α and $\hat{\psi}$ are the effective earth–elasticity factor and the earth tidal potential, respectively. τ_b is the bed shear stress computed using a Manning friction law (Eq. (10)):

$$\vec{\tau}_B = \rho_w \frac{g \cdot n^2}{\sqrt[3]{H}} \cdot \vec{U}^2 \quad (10)$$

where H is the total water depth and n is the Manning coefficient set to 0.020 after calibration of the tidal model. τ_b can also depend on short waves following the approach of Soulsby (1997, Eq. (11)):

$$\vec{\tau}_B = \vec{\tau}_c \left[1 + 1.2 \left(\frac{\vec{\tau}_w}{\vec{\tau}_c + \vec{\tau}_w} \right) \right]^{3.2} \quad (11)$$

where τ_c is the current-induced shear stress and τ_w is the wave-related shear stress computed according to Swart (1974). For a consistent comparison with the case where waves are not considered in the bed shear stress, τ_c is computed using the Manning approach of (Eq. (10)).

Finally, $\vec{\tau}_s$ is the surface stress computed using a bulk formula:

$$\vec{\tau}_s = \rho_a \cdot C_d \cdot \vec{U}_{10}^2 \quad (12)$$

where C_d is a drag coefficient computed according Pond and Pickard (1998). Alternatively, the surface stress can be wave-dependent through the wind friction velocity U_* computed by WWMII as described in Section 2.1.2:

$$\vec{\tau}_s = \rho_a \cdot u_*^2 \quad (13)$$

Over the whole domain, SELFE is forced by hourly fields of sea-level atmospheric pressure and 10 m wind speed originating from the operational high resolution model of ECMWF. The model is forced by the astronomic tidal potential over the whole domain for the tidal constituents MM, MF, O1, K1, P1, Q1, M2, S2, N2 and K2. Along its open boundaries, SELFE is forced by the 18 main tidal constituents in the region (Z0, O1, K1, P1, Q1, M2, S2, N2, K2, 2N2, L2, MU2, NU2, M3, M4, MS4, MN4 and M6), obtained by linear interpolation from the regional tidal model of Pairaud et al. (2008). This representation of the tidal forcing together with a uniform Manning coefficient yields good tidal predictions, with a root mean square error on the total elevation ranging from 0.05 to 0.10 m in the study area, which is slightly better than Bertin et al. (2012), who employed a space-uniform quadratic bottom friction.

2.2. Wave and water level observations

Water levels were collected at three tide gauges available in the studied area for both storms (Fig. 2) through the REFMAR portal (<http://refmar.shom.fr/>). These data consist of 10-min time series over 2010–2011 and were first processed through harmonic analysis using T_Tide (Pawlowicz et al., 2002). A harmonic synthesis was then performed, using the 67 main astronomic constituents. The constituent S_a was not considered in the tidal prediction since, in the North-East Atlantic Ocean, it originates from a combination of thermo-steric and atmospheric effects (unpublished yet). The storm surge was finally computed as the difference between the observed water level and the tidal prediction obtained through this procedure. Deepwater wave conditions in the Bay of Biscay were characterized by means of a non-directional buoy operated by Météo France and the UK met Office (Fig. 2A; Biscay), which provides hourly time-series of significant wave height (H_s), and mean wave period (T_{m02}). In addition, a Datawell buoy was deployed by SHOM (French Naval Oceanographic Service) to the West of Oléron Island (Fig. 2B) during the winter 2010 and provides time series of H_s , T_{m02} , peak wave direction (P_{dir}) and Peak wave period (T_p). Other intermediate water depth buoy observations were available in the Southern part of the Bay of Biscay, such as those of Cap ferret and Anglet, operated by CETMEF (<http://candhis.cetmef.developpement-durable.gouv.fr>) and that of Bilbao operated by Puerto del Estado (<http://www.puertos.es>). Other coastal buoy observations are available in the Bay of Biscay farther from the study area but the spatial resolution of our computational grid and the bathymetric data at our disposal prevent a consistent comparison with our modeling results.

3. The studied area and storms

3.1. Geomorphic setting

The study area corresponds to the Central part of the Bay of Biscay and the geomorphology of the coast is dominated by two big islands and several embayments and estuaries, the major being the Gironde Estuary to the South (Fig. 2). These embayments

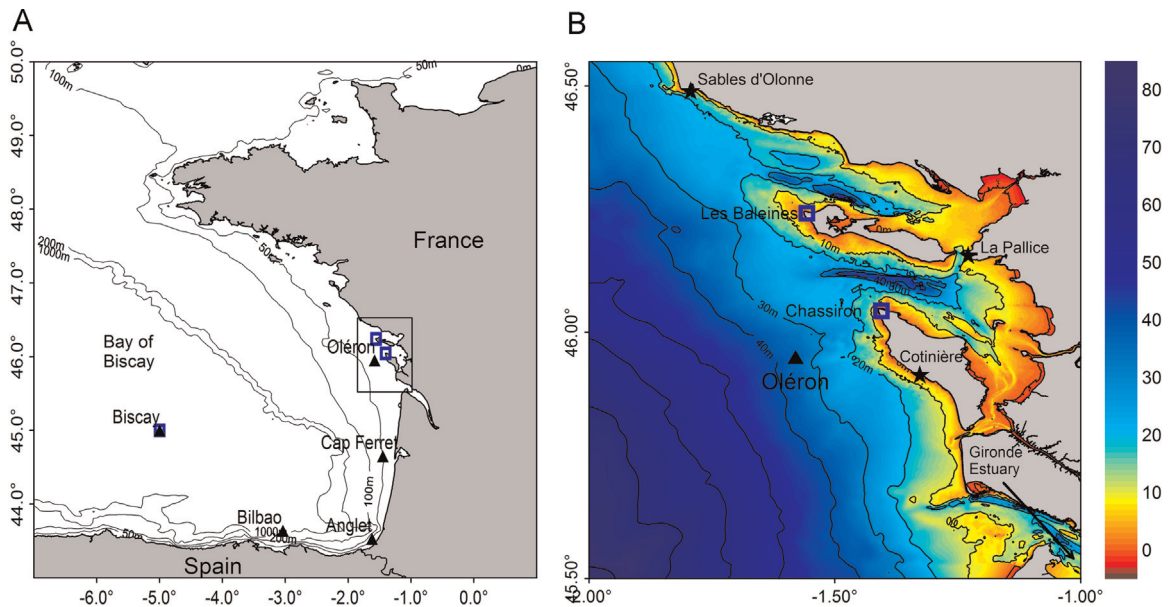


Fig. 2. (A) Location of the study area in the Bay of Biscay and (B) detailed bathymetric map of the study area with respect to mean sea-level with the location of tide gauges (stars), wave buoys (triangles) and meteorological stations (squares) used in this study.

correspond to drowned incised valley segments (Chaumillon et al., 2008) and their inner part consists of extensive intertidal mudflats, locally reaching 5 km width and bounded by dykes and natural barriers. These barriers isolate extensive marshes and coastal plains, some of which include large areas located below the high astronomical tidal level (Breilh et al., 2013). Most of these dykes were flooded and/or breached during Xynthia, which caused severe human and material losses (Breilh et al., 2013; André et al., 2013). The continental shelf in this area is wide and ranges from about 100 km to the South of the Gironde Estuary to 170 km to the North of Ré Island (Fig. 2).

3.2. Hydrodynamic setting

Tides in the study area are semi-diurnal, with small diurnal asymmetries. Along the shelf break, the deep-water Kelvin wave induces a M2 wave with amplitude of the order of 1.3 m (Le Cann, 1990), which grows up to more than 1.8 m in the inner part of the estuaries.

Diurnal waves K1 and O1 have amplitudes of the order of 0.07 m and display little spatial variations. In contrast, the amplitudes of quarter diurnal waves M4, MS4 and MN4 are amplified more than 10 times throughout their propagation over the central part of the continental shelf. This interesting phenomenon was explained analytically by Le Cann (1990) and then confirmed numerically by Bertin et al. (2012), who showed that the resonant frequency of the shelf in the central part of the Bay of Biscay was close to the frequency band of the quarter diurnal constituents. The resulting spring tidal range at the coast exceeds 6 m in the inner part of the estuaries and the associated tidal currents can exceed 2 m/s (Bertin et al., 2005).

The Bay of Biscay is fully exposed to short-waves generated in the North Atlantic Ocean. Due to the scarcity of wave data offshore of the study area, the long term hindcast of Dodet et al. (2010) is used to characterize the local wave climate. The annual-mean

deep water significant wave height (H_s) is of the order 2.0 m and the mean directions and peak period are 10 s and 285°, respectively. Winter storms can episodically produce waves of H_s larger than 10 m. During their propagation over the broad continental shelf, waves experience a significant attenuation of H_s and a strong refraction, which limit wave obliquity along the coast (Bertin et al., 2008). Winter-mean wave conditions in the Bay of Biscay experience a significant inter-annual variability, which was shown by Dodet et al. (2010) to be partly controlled by the North Atlantic Oscillation.

3.3. The studied storms

The first storm, Xynthia, hit the central part of the Bay of Biscay in the night of the 27th to the 28th of February 2010. Xynthia originated from a low-pressure zone located in the middle of the Atlantic Ocean around the latitude of the Tropic of Cancer. This depression intensified on the 27th in the morning and evolved towards a storm when reaching the coastlines of Portugal (Fig. 3). Xynthia crossed the North-Western part of Spain and hit the French border of the Bay of Biscay in the night of the 28th of February, where sea-level pressure (SLP) reached its minimum at 969 hPa (Fig. 3). Southern to South-Western winds ranging from 25 to 30 m/s (hourly-mean 10 m wind speed, hereafter U_{10}) blew over the Southern part of the Bay of Biscay (Fig. 3). Maximum instantaneous gusts reached 45 m/s at Les Baleines (Fig. 2). Such wind speed are not exceptional for the region since over the last 15 years, storms Martin (27th of December 1999) and Klaus (23th January 2009) produced gusts over 50–55 m/s. Much more unusual was the track of Xynthia from SW to NE (Rivière et al., 2012). Wave measurements in the Bay of Biscay showed that H_s during Xynthia ranged from 6 to 7.5 m, which values are regularly encountered during winter storms. Nevertheless, Xynthia induced an exceptional storm surge, estimated to more than 1.5 m in La Pallice (Fig. 2), which corresponds to the largest value since the

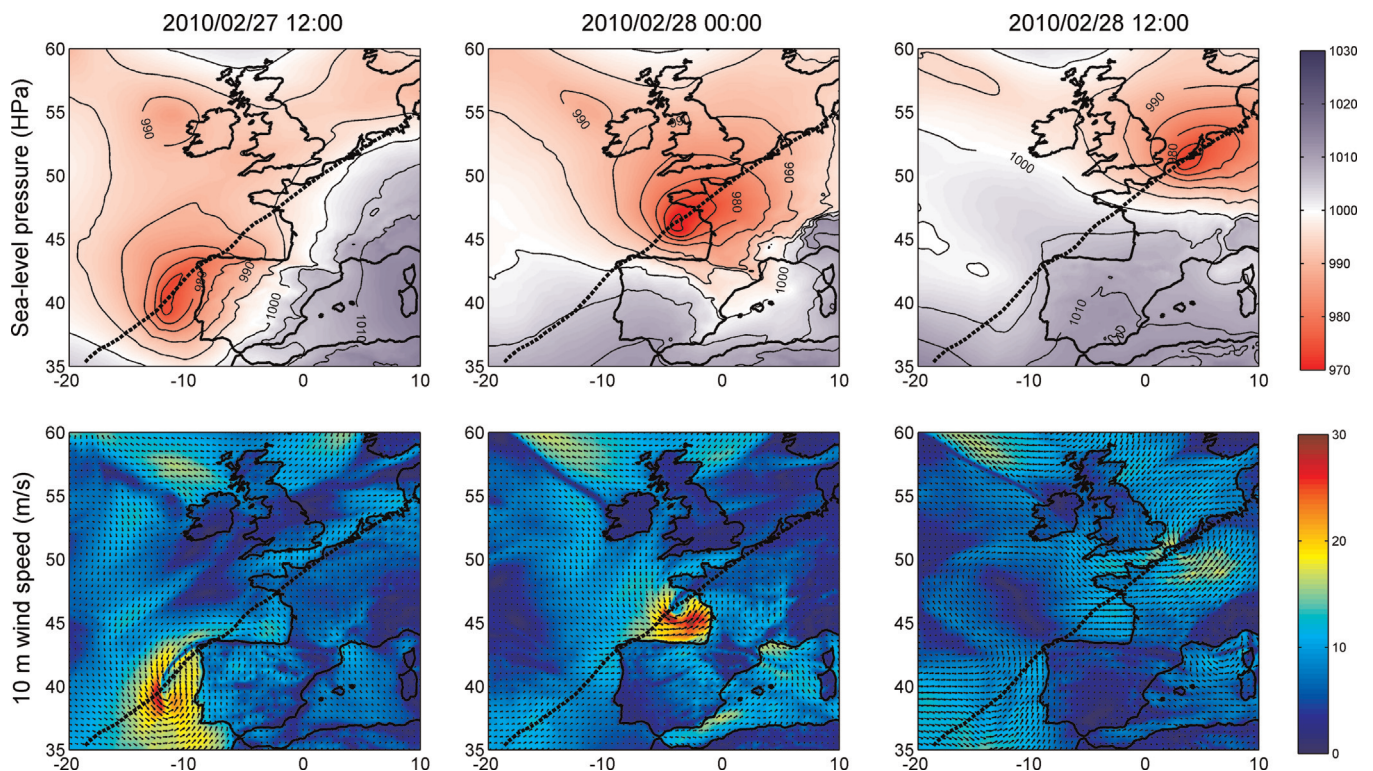


Fig. 3. Sea-level pressure (hPa) and 10 m wind speed (m/s) during Xynthia based on the operational analysis of ECMWF. The dashed line corresponds to the track of the minimum sea level pressure.

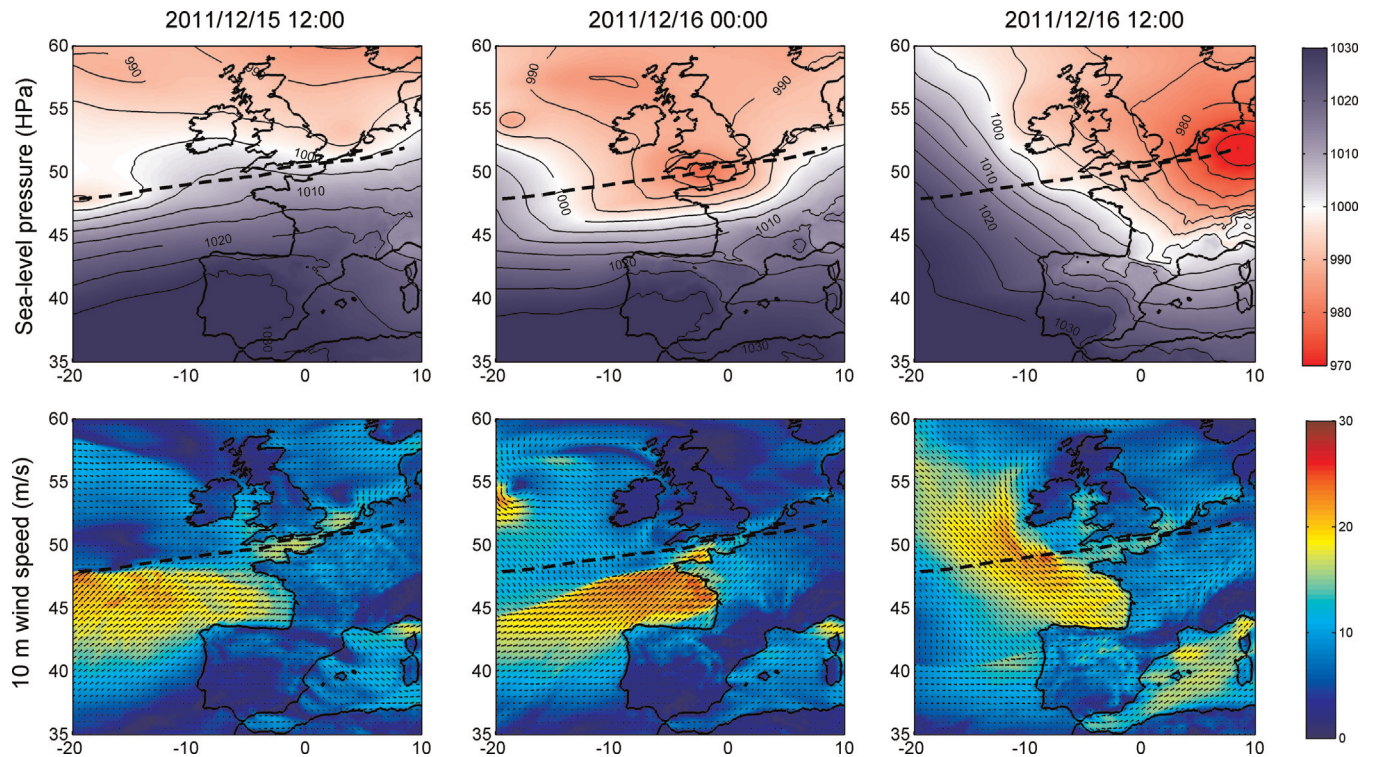


Fig. 4. Sea-level pressure (hPa) and 10 m wind speed (m/s) during Joachim based on the operational analysis of ECMWF. The dashed line corresponds to the track of the minimum sea level pressure.

installation of a permanent tide gauge at this station in 1997. This large storm surge peaked at the same time as a high spring tide (5.9 m tidal range in La Pallice) and the subsequent exceptional water level caused the flooding of extensive low-lying coastal zones, damage of more than 2 billion Euros and 47 fatalities, 41 of which occurred in flooded areas (André et al., 2013). Through a preliminary application of a storm surge model at the scale of the continental shelf, Bertin et al. (2012) showed that this exceptional storm surge resulted mainly from a particular sea-state during Xynthia, characterized by short-period waves which enhanced the ocean surface roughness. These authors also showed that tide-surge interactions were limited in the study area and impacted the storm surge by less than 0.1 m during Xynthia (Bertin et al., 2012).

The second storm, Joachim, hit the Bay of Biscay in the night of the 15th to the 16th of December 2011. The track of Joachim roughly followed the English Channel where the minimum SLP evolved around 975 hPa. South-Western winds blew over a large fetch across the Bay of Biscay with U_{10} of the order of 25 m/s. In the study area, maximum gusts of the order of 40 m/s were recorded at Les Baleines (Fig. 2). Joachim induced a moderate storm surge, which ranged between 0.7 and 1.05 m in the study area, which values are locally two times lower compared to Xynthia. The storm lasted more than 12 h (i.e. wind speed > 20 m/s) and therefore encompassed a full tidal cycle, but peaked at high tide for moderate tidal ranges (3.75 m tidal range in La Pallice). Wave measurements in the Bay of Biscay revealed H_s larger than 10 m during Joachim. The maximum storm surge peaked during intermediate tidal range so that damages were limited in the study area.

4. Modeling results

4.1. Atmospheric forcing

Fields of sea-level pressure (SLP) and 10 m winds (U_{10})

originating from the operational high resolution forecast model of ECMWF were compared against field observations available during both storms in the study area (Fig. 2). The model data consist of successive hourly forecasts from 0 and 12 UTC, with a horizontal resolution of 16 km. This comparison reveals firstly that SLP is very well predicted for both storms, with a Root Mean Square Discrepancy (hereafter RMSD) of the order of 1.5 hPa (Fig. 5). Note that it was found necessary to use hourly output from ECMWF rather than 3 hourly as was originally available for Xynthia.

Modeled wind speed and direction were also compared against measurements at the same sites and this comparison reveals that for both storms, wind speed is reasonably predicted with a RMSD of the order of 2 m/s (Fig. 6). However, it should be noted that the height at which the measurements are taken differs from the 10 m reference height of the model at two stations. Thus, wind is measured at 17 m at Les Baleines and 3 m at Biscay (Fig. 2). Such differences directly explain the positive bias of the model at Biscay and the negative bias at Les Baleines. Measurements could have been adjusted assuming a logarithmic profile, however, such a correction implies a hypothesis on the roughness length Z_0 , which determination is one of the objectives of this study. Wind direction is reasonably reproduced with a RMSD ranging from 15° to 20°.

4.2. Wave predictions

Wave predictions were compared against the measurements available for both storms in the Bay of Biscay and model data comparison is shown for Biscay and Datawell Oléron stations (Figs. 7 and 8). For Xynthia, this comparison reveals that H_s is well reproduced with a RMSD ranging from 0.31 to 0.44 m, corresponding to a 11–16% error once normalized by the observations (NRMSD, Table 1). It is worth noting that H_s during Xynthia were not exceptional since two events produced equivalent wave height in the same week. The drops in wave peak direction and period are also well captured, although with a 2 h delay. Finally, the mean wave period T_{m02} is very well reproduced with a RMSD of 0.7–0.9

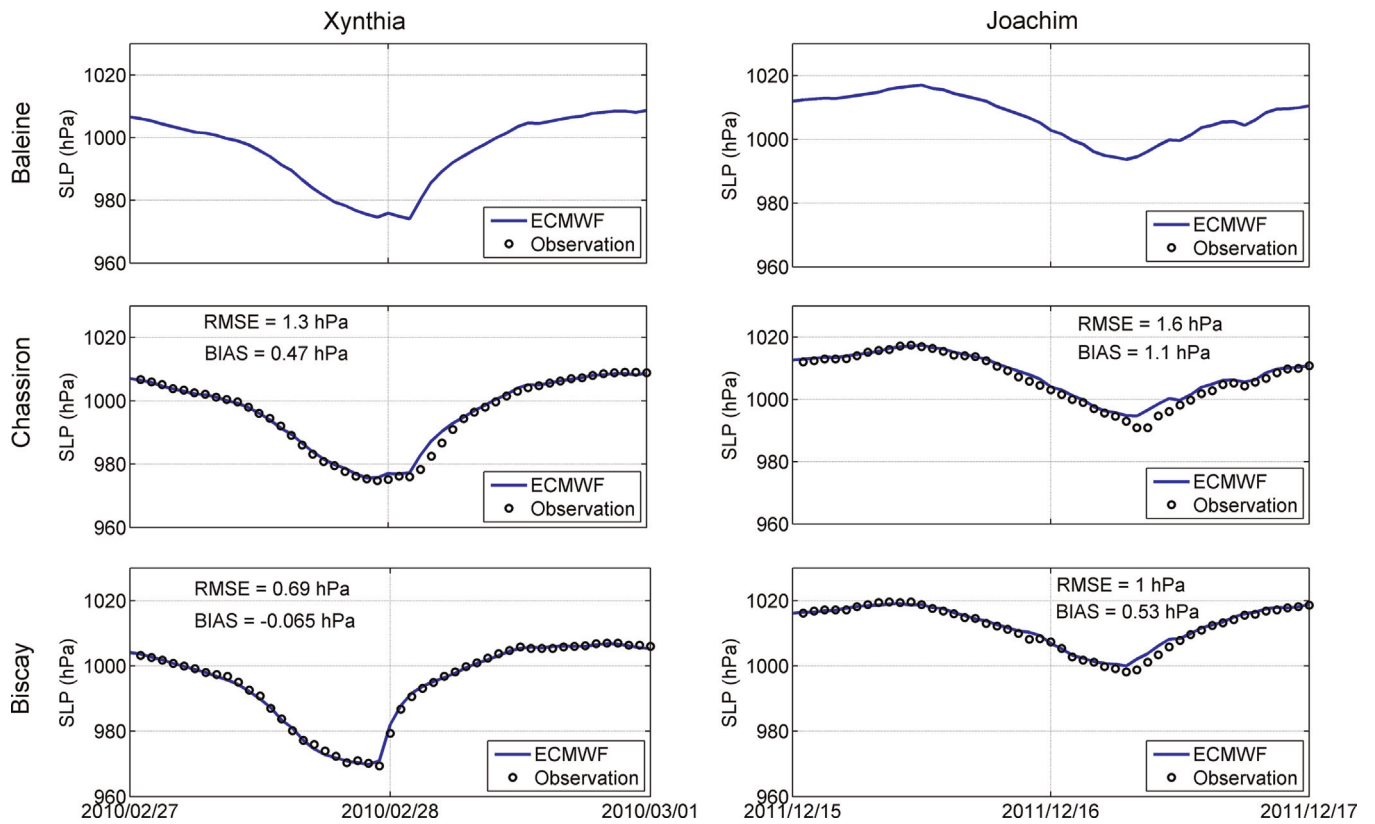


Fig. 5. Modeled against observed sea-level pressure at Les Baleines, Chassiron and Biscay stations during both storms.

for all stations, which yields a 10% NRMSD (Table 1, Fig.7). Both model and observations reveal that T_{m02} is temporarily higher than T_p at the beginning of Xynthia while the values for these

parameters range from 10 to 11 s at the storm peak. Such short-period waves with H_s larger than 7 m correspond to a young sea state with steep waves.

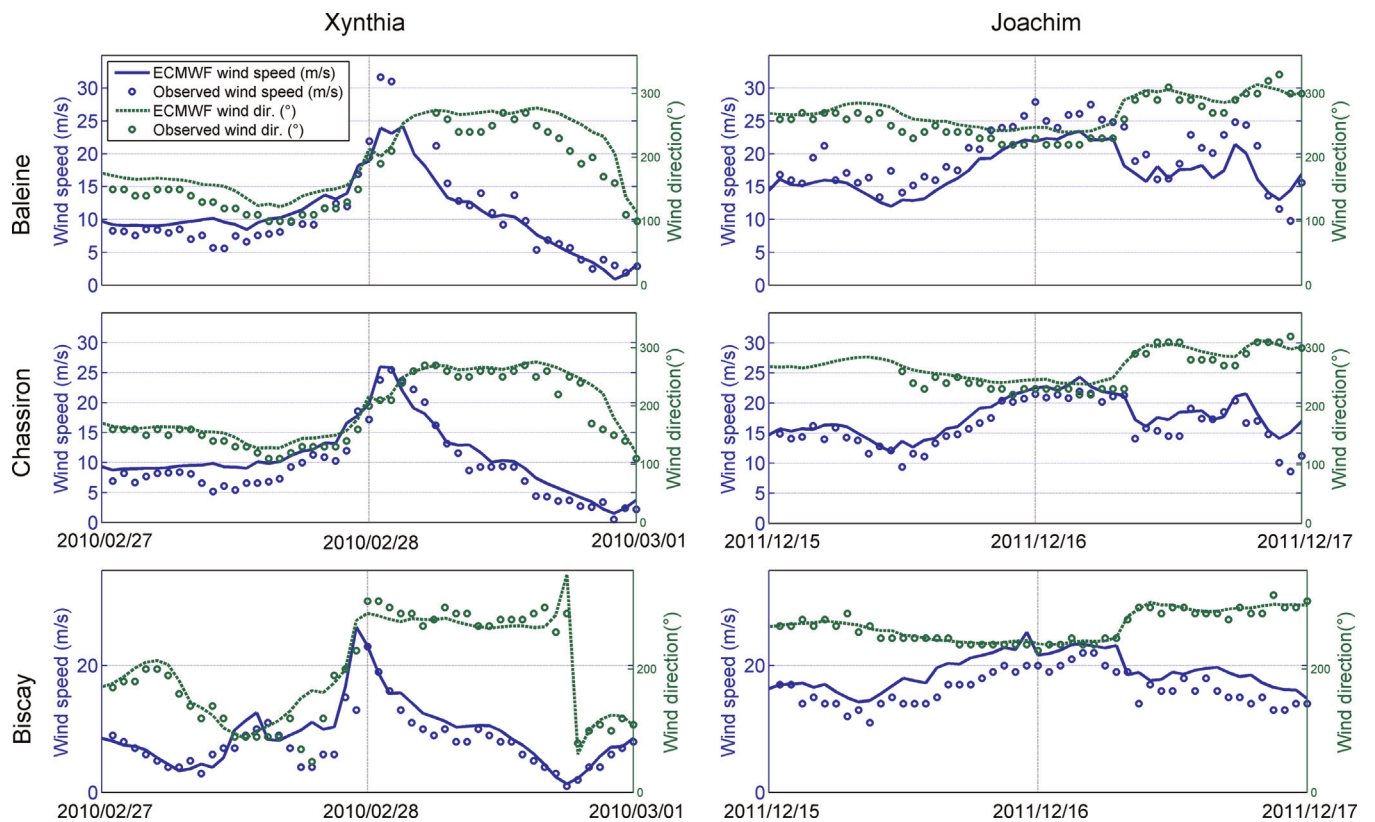


Fig. 6. Modeled against observed wind speed and direction at Les Baleines, Chassiron and Biscay stations for both storms.

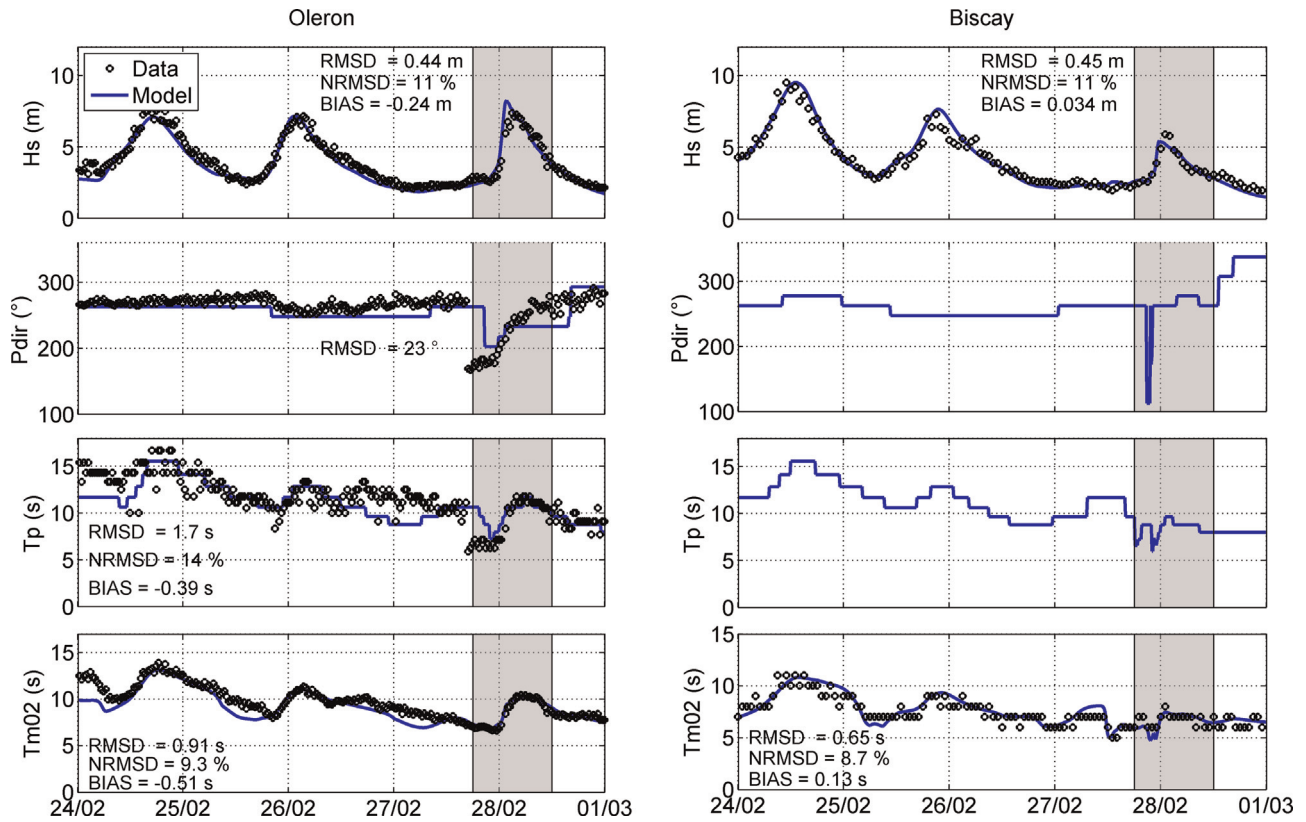


Fig. 7. Observed against modeled wave parameters at Oléron and Biscay buoys during Xynthia.

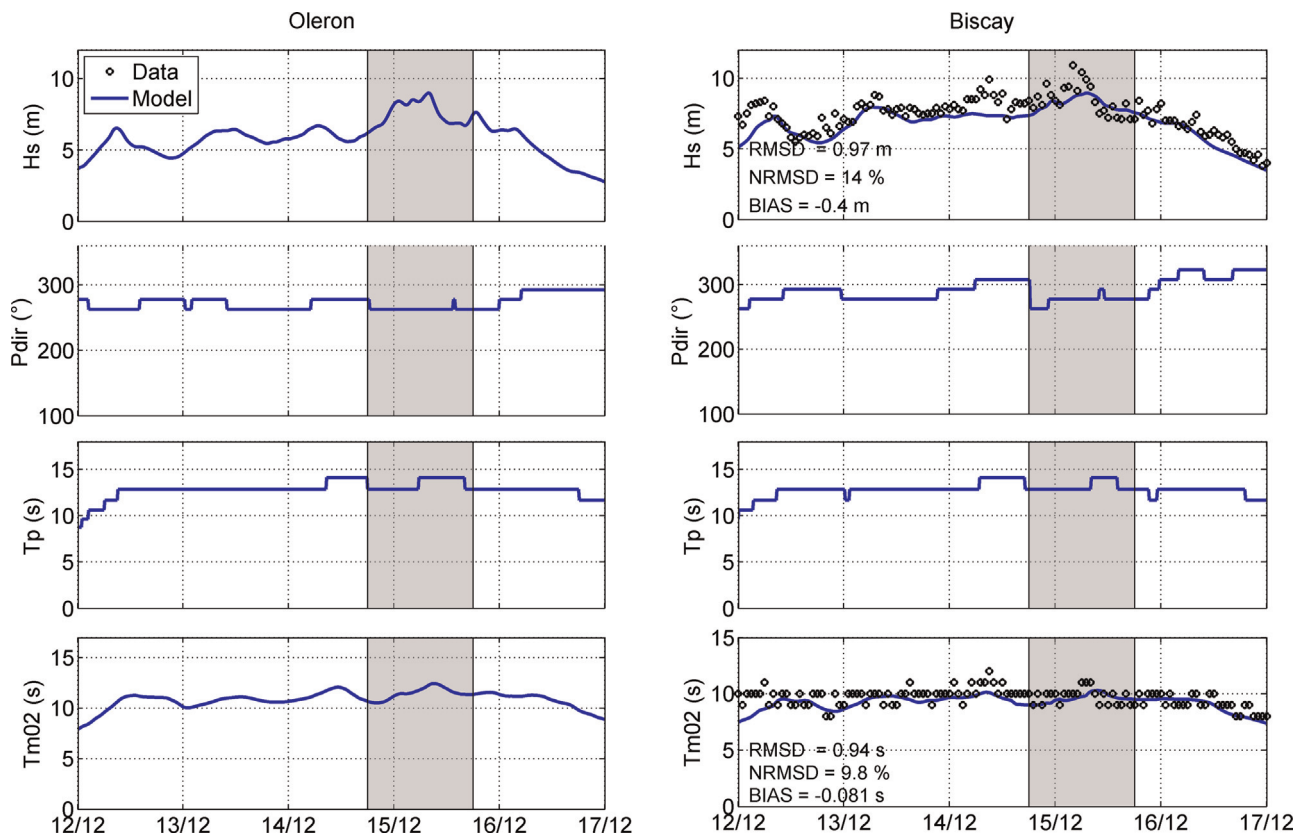


Fig. 8. Observed against modeled wave parameters at Oléron and Biscay buoys during Joachim.

Table 1

Statistical errors (Root Mean Square Discrepancy, Normalized Root Mean Square Discrepancy and Bias) for the significant wave height (H_s), the peak wave period (T_p), the mean wave period (T_{m02}) and the mean wave direction (Mwd) at the available buoys for Xynthia and Joachim. Na denotes non-available data.

Name	Buoy ID	Storm	H_s			T_p			T_{m02}			Mwd
			RMSD (m)	NRMSD (%)	BIAS (m)	RMSD (s)	NRMSD (%)	BIAS (s)	RMSD (s)	NRMSD (%)	BIAS (s)	RMSD (deg)
Biscay	62001	Xynthia	0.35	12	-0.05	Na	Na	Na	0.8	12	0.2	Na
		Joachim	0.88	11	-0.35	Na	Na	Na	0.7	7	-0.2	Na
Oléron		Xynthia	0.44	11	-0.24	1.7	14	-0.4	0.9	9.3	-0.5	23
		Joachim	Na	Na	Na	Na	Na	Na	Na	Na	Na	Na
Cap Ferret	62064	Xynthia	Na	Na	Na	Na	Na	Na	Na	Na	Na	Na
		Joachim	0.59	9	0.3	Na	Na	Na	0.9	7.4	-0.6	Na
Anglet	62066	Xynthia	0.31	14	0.12	2	22	0.38	0.8	12	0.18	Na
		Joachim	0.91	16	-0.34	1.2	9.5	0.9	Na	Na	Na	Na
Bilbao	62024	Xynthia	0.38	16	0.2	Na	Na	Na	0.7	11	0	19
		Joachim	1.1	18	-0.48	Na	Na	Na	0.7	7	0	8

Joachim induces more energetic waves in the Bay of Biscay, with H_s temporarily exceeding 10 m at the storm peak. These waves are reproduced by our modeling system with a comparable accuracy as for Xynthia (9–18% NRMSD, Table 1, Fig. 8), although with a negative bias of the order of 0.4 m. The peak wave period was only available at Anglet and was of the order of 14–15 s, which values were adequately reproduced with a RMSD of the order of 1 s. The mean wave period T_{m02} was of the order of 10–11 s and was reproduced with a 7% error (Table 1, Fig. 8). The MWD was only available at Bilbao and was very well reproduced with a RMSD of 8°. According to the model, the MWD was quite homogeneous in the southern part of the Bay of Biscay and was of the order of N270°. Considering 10–20 year records at the available buoys in the Bay of Biscay, the values met during Joachim correspond to typical values for the Bay of Biscay.

4.3. Storm surge predictions

For both storms, modeled storm surges were computed as the difference between our baseline simulation (Table 2, configuration 1) and a tide-only simulation. Model predictions were compared against observations at Sables d'Olonne, La Pallice and La Cotinière stations (Fig. 2). For Xynthia, a comparable accuracy can be observed at La Pallice and La Cotinière with a RMSD of 0.12–0.15 m while the storm surge is slightly better reproduced at Les Sables d'Olonne with a RMSD of 0.08 m (Fig. 9). In detail, the model slightly over-estimates the surge peak at La Cotinière. For the three stations, the model displays a 0.05–0.15 m negative bias during the 12 h period preceding the storm. For Joachim, the storm surge is predicted with a comparable level of accuracy although the model displays a 0.05–0.10 m negative bias both at Sables d'Olonne and La Pallice (Fig. 9). The tide gauge at La Cotinière was not operating during this storm.

5. The contributions of short-waves in storm surges

Although both storms induced winds of comparable speed and

Table 2

Settings of the numerical experiments performed to investigate the contribution of wave-induced processes.

Simulation number	Wave-dependent surface stress	Gradients of wave radiation stress	Wave-dependent bottom stress
1	Yes	Yes	Yes
2	No	Yes	Yes
3	Yes	No	Yes
4	Yes	Yes	No

direction, the resulting storm surges in the central part of the Bay of Biscay were up to two times larger during Xynthia than Joachim. The slightly higher winds during Xynthia can only explain a small part of these differences. By contrast, the sea states were very different for both storms, with moderately large but short period waves during Xynthia and very large and longer period waves during Joachim. These contrasting settings provide a unique opportunity to investigate the contribution of short waves in storm surges. This section presents numerical experiments that aim at better understanding the respective contributions of three wave-induced processes: (1) wave-increased surface stress; (2) gradients of wave radiation stress and (3) wave-increased bottom stress. The settings of these numerical experiments are summarized in Table 2.

5.1. Wave enhancement of surface stress

In order to evaluate the importance of short waves on the magnitude of the surface stress, we compared storm surges computed with a wave-dependent formula (simulation no. 1, Table 1) and with the bulk formula of Pond and Pickard (1998) (simulation no. 2, Table 1). For Xynthia (Fig. 10), the wave-dependent approach yields a 20–25% larger surge at Sables d'Olonne and La Cotinière and a 35% larger surge at La Pallice while this approach much better matches the observations. For Joachim, the two approaches yield differences of the order of 2% at Sables d'Olonne and La Cotinière while the storm surge is 10–15% larger at La Pallice using a wave dependent approach (Fig. 10).

The maximum difference between both simulations was also computed for each grid node to provide a spatial overview of these differences (Fig. 11). This figure confirms firstly that much larger differences are obtained for Xynthia than for Joachim. For Xynthia, maximum differences grow from less than 0.25 m at the entrance of the estuaries to more than 0.5 m in shallow bays while for Joachim, differences are only significant in the inner part of the shallow bays where they reach 0.1–0.2 m. The increase in differences from intermediate water depth (e.g. 20–30 m) to the shallower part of the study area is explained by a larger contribution of the surface stress in the overall storm surge, because the effect of the surface stress is inversely proportional to the water depth.

To better understand why differences between both approaches are much larger for Xynthia than for Joachim, time series of energy spectra, wave age and surface stress were extracted at the location of the Datawell buoy (Fig. 2B) and plotted on Fig. 12. This comparison shows that for Xynthia, the surface stress is up to two times larger with the wave dependent approach compared to the bulk formula (Fig. 12). Such differences suggest that a particular sea-state occurred during Xynthia. Indeed, wave measurements as well as model results showed that, a few hours before

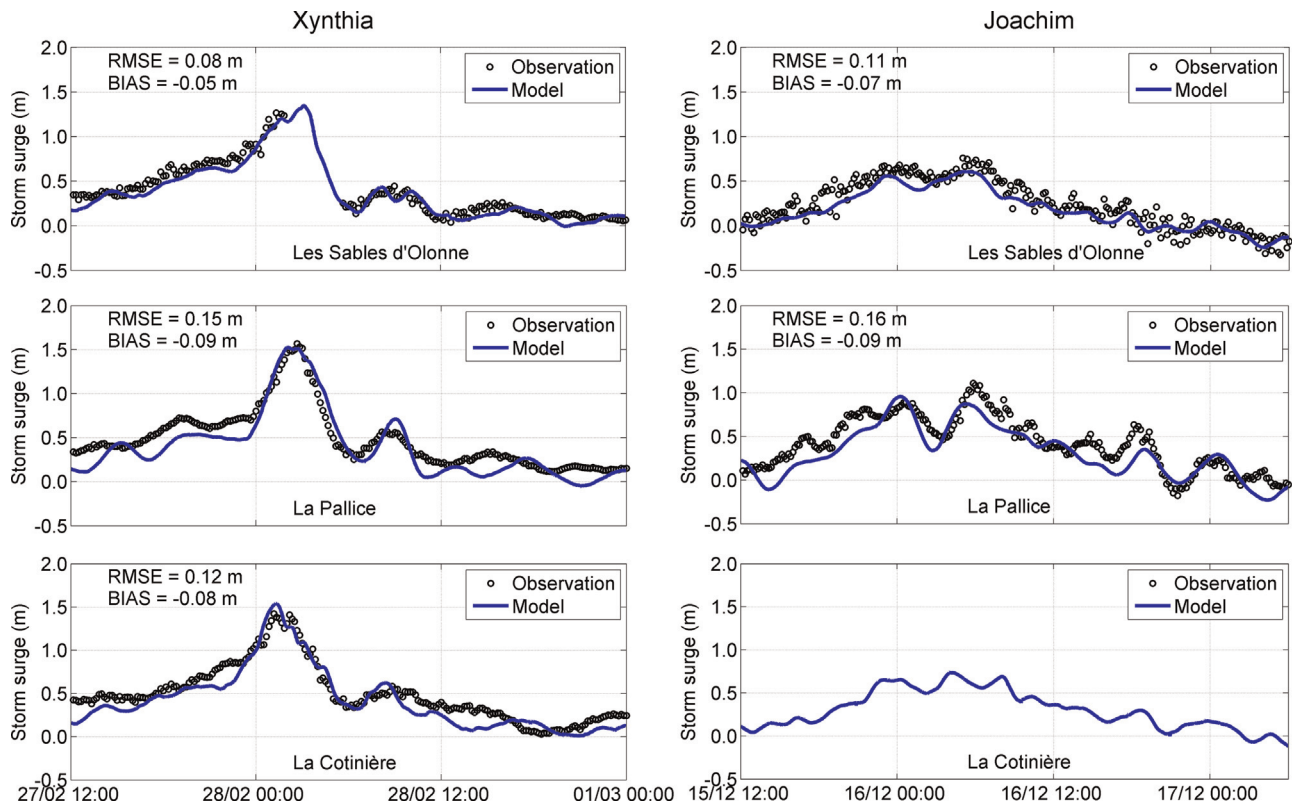


Fig. 9. Modeled against observed storm surges at Sables d'Olonnes, La Pallice and La Cotinière stations for storms Xynthia and Joachim.

the storm peak, H_s ranged from 4 to 6 m with T_p ranging from 6 to 8 s (Fig. 7). The mean wave period T_{m02} even temporarily exceeded T_p during this stage of the storm and the wave age dropped to

7 during Xynthia, which is two times less than Joachim. Time-series of energy spectra (Fig. 12a) show that, during this period, a lot of energy was found in the range 0.10–0.15 Hz, with spectral

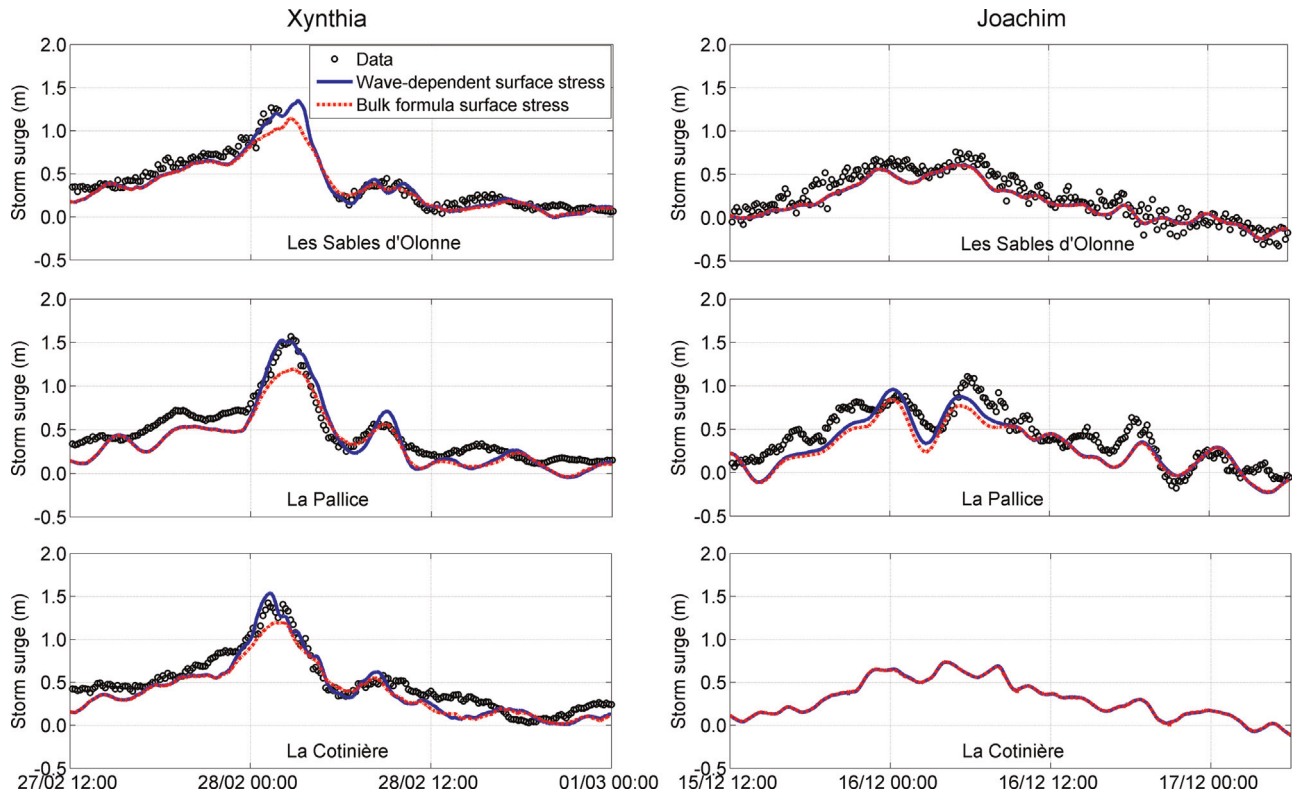


Fig. 10. Observed (black circles) against computed storm surges using a wave dependent (blue) and a bulk formula (red) at Sables d'Olonne, La Pallice and La Cotinière for storms Xynthia and Joachim. (For interpretation of the references to color in this figure legend, the reader is referred to the web version of this article.)

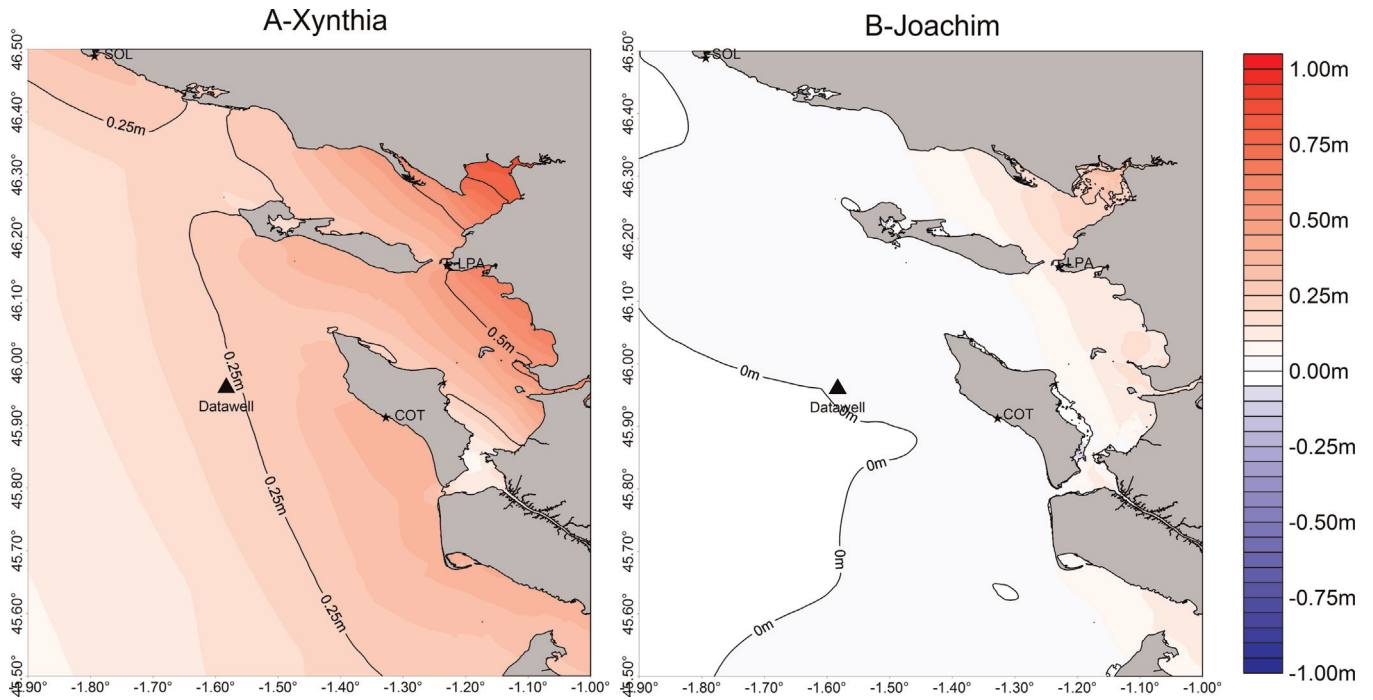


Fig. 11. Maximum difference in surface elevation between a simulation employing a wave-dependent surface stress and a surface stress computed from the bulk formula for (A) Xynthia and (B) Joachim.

density reaching $70 \text{ m}^2 \text{ Hz}^{-1}$. This spectral repartition strongly differs for Joachim, where maximum energy in this frequency band reaches $30 \text{ m}^2 \text{ Hz}^{-1}$, although the total energy was much larger. Such conditions during Xynthia are representative of a very young sea state. The parameterization employed to compute the wind input source terms in the wave model (Section 2.1.2) implies that the high energy levels at high frequencies caused the friction

velocity to be very large. Hence, the particular sea state that developed during Xynthia directly explains the two times larger surface stress compared to bulk formula approach. Moreover, it can be clearly seen that during Joachim, the energy spectral repartition varies little throughout the storm whereas for Xynthia, there is very abrupt growth of spectral energy after a quite calm period that leads to this high energy levels in the short wave range

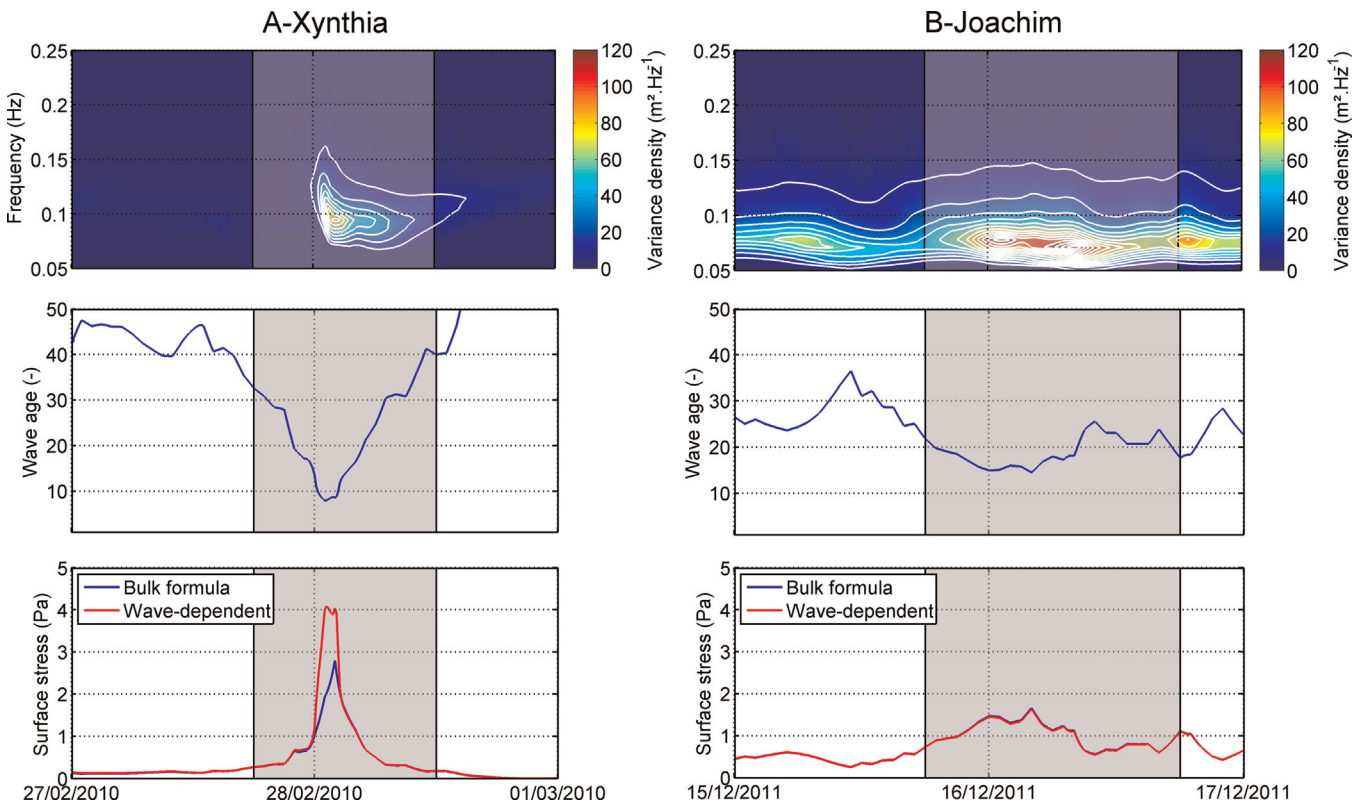


Fig. 12. Time series of energy spectra ($\text{m}^2 \text{ Hz}^{-1}$), wave age (dimensionless) and surface stress (Pa) for Xynthia (A) and Joachim (B).

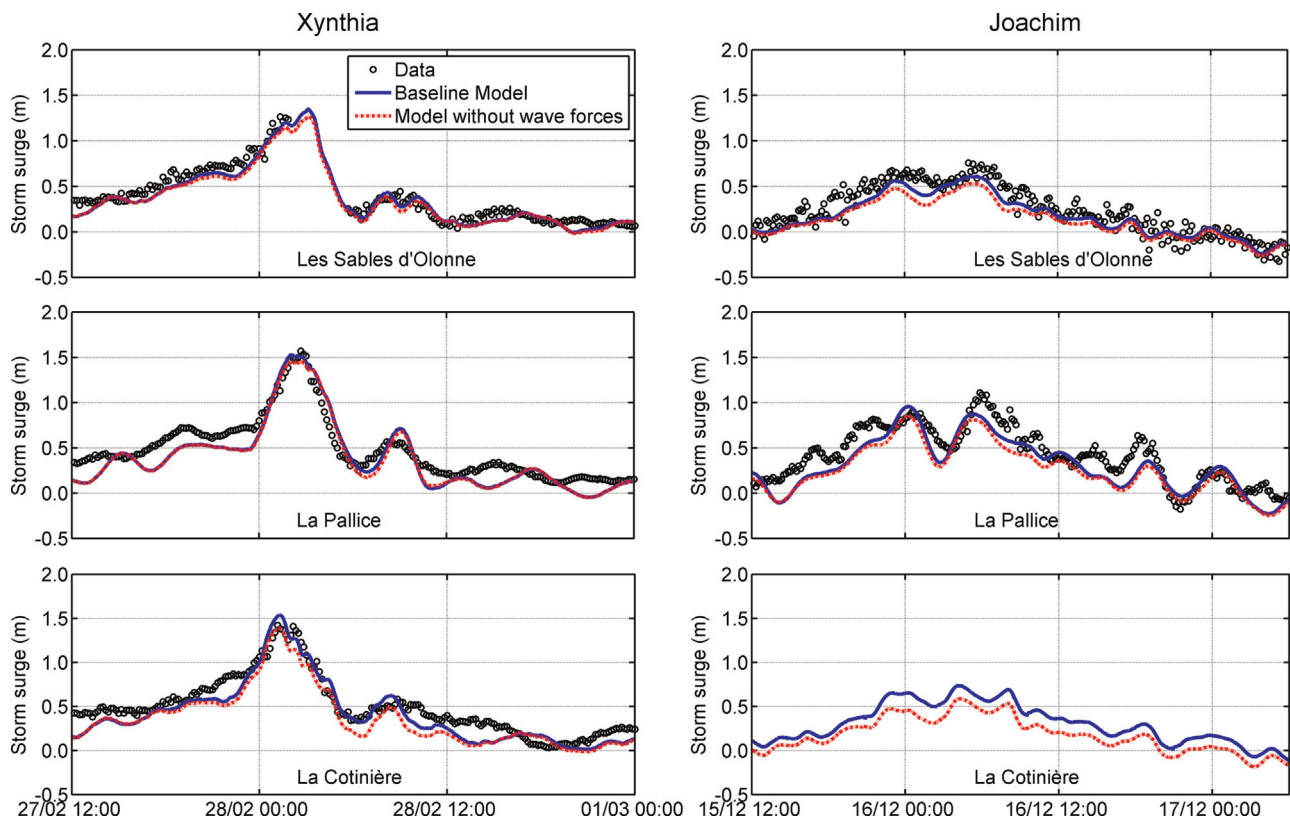


Fig. 13. Observed (black circles) against computed storm surges with (red) and without radiation stress (blue) at Sables d'Olonne, La Pallice and La Cotinière for storms Xynthia and Joachim. (For interpretation of the references to color in this figure legend, the reader is referred to the web version of this article.)

of the spectra.

The large differences in sea state between Xynthia and Joachim are proposed to be associated with the tracks of these storms. Joachim followed a classical track W–E, implying a fetch of a few thousands of km, which resulted in large and long period waves. By contrast, Xynthia followed an unusual SW–NE track, which restricted the fetch to a few hundreds of kilometers and resulted in a much younger sea state.

5.2. Wave-induced forces

Wave dissipation in the nearshore induces gradients of radiation stress (Longuet-Higgins and Stewart, 1964), which drive a setup along the coast (Bowen et al., 1968). To investigate the contribution of this phenomenon in the overall storm surge, the difference between a simulation with radiation stress and a simulation without radiation stress was computed for both storms (Table 1, simulation 3). Surprisingly, the differences between both approaches are not negligible at the three considered tide gauges, although being located in harbors sheltered from wave breaking. Maximum differences are found at La Cotinière, where they reach 0.15 m during Xynthia and 0.2 m during Joachim. For the three stations, accounting for wave radiation stress improves storm surge predictions noticeably (Fig. 13).

To provide a spatial overview of this phenomenon, the maximum difference between both simulations was also computed for each grid node (Fig. 14). This figure reveals firstly that maximum setup develops along the western side of the islands and shorelines exposed to the Ocean. A zoom reveals that to the North of Oléron Island (Fig. 2B), maximum setup locally exceeds 0.3 m during Xynthia and 0.4 m during Joachim. However, it is expected that the maximum spatial resolution of our computational grid (25 m) is not sufficient to capture the maximum setup along the

coastlines. This problem may be enhanced during Xynthia because the very high water levels at the storm peak have caused the breaking zone to end up over the dikes and dunes. The proper representation of wave breaking over such steep barriers would imply employing a much finer spatial resolution (e.g. # 1 m), which is outside the scope of this study. Secondly, several studies suggested that for energetic conditions, wave induced-turbulence and bottom stress related to bed return flow could increase wave setup along the coastline significantly (e.g. Aptsos et al., 2007; Bennis et al., 2014). Such phenomenon cannot be accounted for properly with a 2DH approach, which would suggest that our setup predictions are locally under-estimated. However, more surprisingly, this comparison also shows the development of a regional setup inside the estuaries, this phenomenon being more significant during Joachim. The regional bathymetry (Fig. 2) implies that wave setup locally reaching 0.2 m develops in water depth of one or several tens of meters, which is typically outside the breaking zones. Our interpretation is that the islands are bounded by extensive shallow shoreface where wave breaking zones develop over several kilometers during storms. This setting causes wave setup to propagate outside these large breaking zones, including the harbors where water levels are measured. A similar phenomenon was already reported in small coastal lagoons by Bertin et al. (2009) and Dodet et al. (2013).

5.3. Wave enhancement of bottom stress

Several studies investigated the impact of wave-enhanced bottom stress on storm surges (Xie et al., 2003; Nicolle et al., 2009) although it is not really clear whether accounting for this process improves storm surge predictions or not (Jones and Davies, 1998). In this context, we took advantage of these two contrasting storms to investigate the contribution of this phenomenon in storm

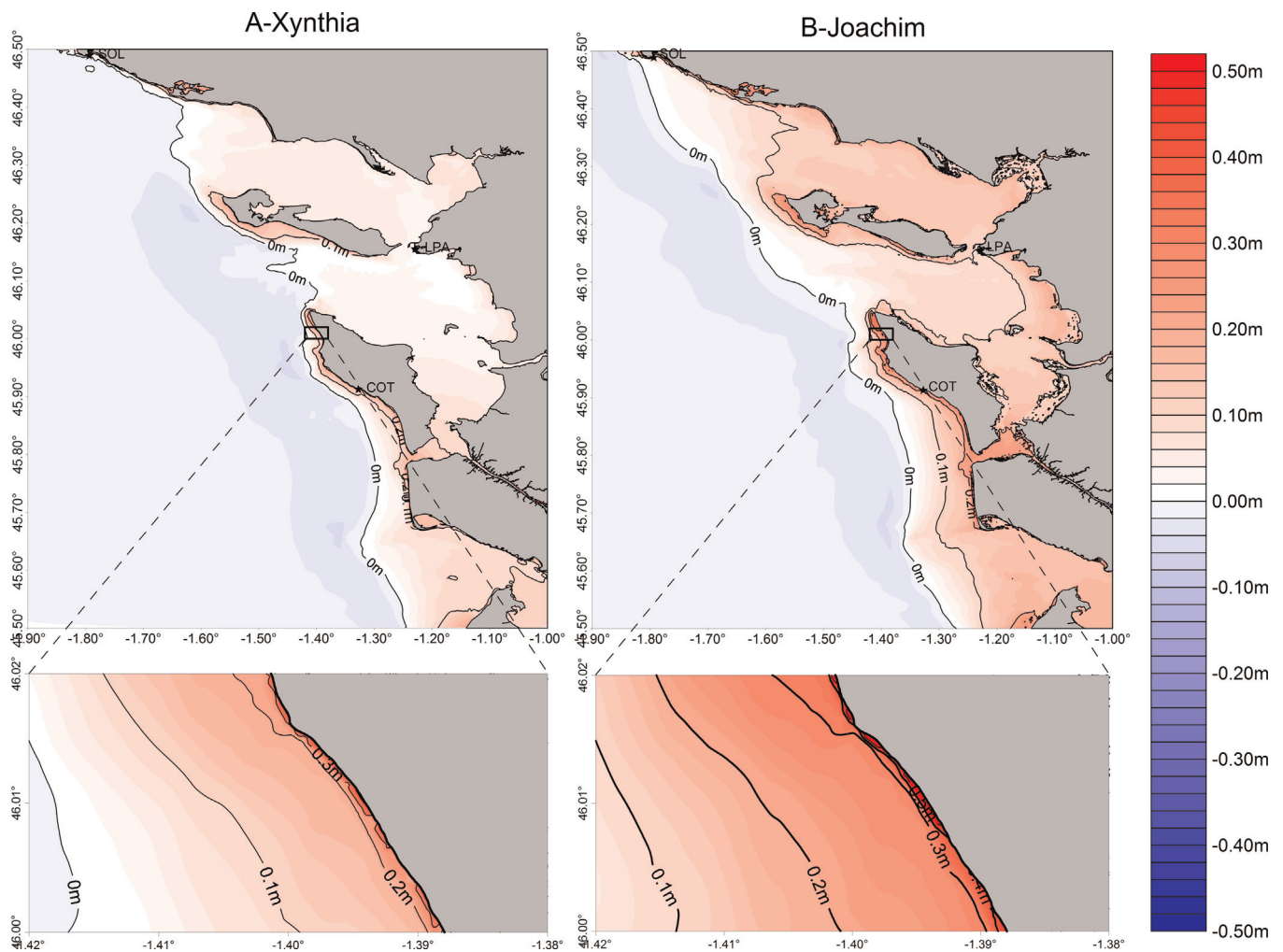


Fig. 14. Maximum difference in surface elevation between a simulation including wave forces and a simulation without wave forces for (A) Xynthia and (B) Joachim.

surges. The comparison between both approaches at the three selected tide gauges revealed very limited differences, with the wave dependent bottom stress generally decreasing the storm surge by 0.05 m (Fig. 15). Such differences are too weak to conclude whether a wave dependent parameterization for bottom stress improves storm surge predictions. Alternative parameterizations, such as that of Grant and Madsen (1979) were also tested but resulted in comparable predictions. In addition, bottom stress parameterization also alters tidal propagation while the modeled storm surge is computed by subtracting water levels originating from a tide-only simulation. Therefore, the observed differences probably also result from tidal propagation differences between both simulations. However, the limited sensitivity on the bottom stress parameterization may be explained by the fact that the selected tide gauges are connected to channels where water depths rapidly reach or exceed 10–20 m, which causes bottom stress to be a second order process. To better investigate this phenomenon, further studies will have to be carried out with water level measurements by much smaller water depth.

6. Conclusions and future work

This study investigated the contribution of short waves in storm surges, based on two storms that hit recently the central part of the Bay of Biscay. Despite displaying comparable wind fields in the study area, these storms induced substantially

different storm surges and sea states.

The comparison between a wave dependent and a bulk formula parameterization to compute the surface stress revealed that the larger-than-normal storm surge during Xynthia was explained by a particular sea-state, characterized by young and steep waves. This particular sea-state, rather uncommon in the North-East Atlantic Ocean, enhanced the surface stress significantly and was explained by the particular track of Xynthia, which reduced the fetch to a few hundred kilometers in the Bay of Biscay. By contrast, employing a wave-dependent surface stress for Joachim did not produce significant differences although waves were much bigger than during Xynthia. These results suggest firstly that a wave-dependent surface stress should be employed for storm surge predictions in small seas such as the Mediterranean, the Adriatic or the Black Sea, where young sea states similar to those produced by Xynthia are much more common. More generally, a wave dependent surface stress parameterization should be preferred in operational storm surge models since it did not deteriorate predictions for more developed sea-states.

The numerical experiments on wave forces revealed that during storms, wave setup can locally exceed 0.4 m along shorelines exposed to large waves. More surprisingly, this analysis showed that a regional setup can also develop outside breaking zones and propagate in the inner part of estuaries. This behavior, which was already shown in shallow wave dominated inlets, will have to be verified in other coastal environments, such as barrier islands, estuaries and rias. However, it is expected that our predictions of wave setup are locally under-estimated, first due to a lack of

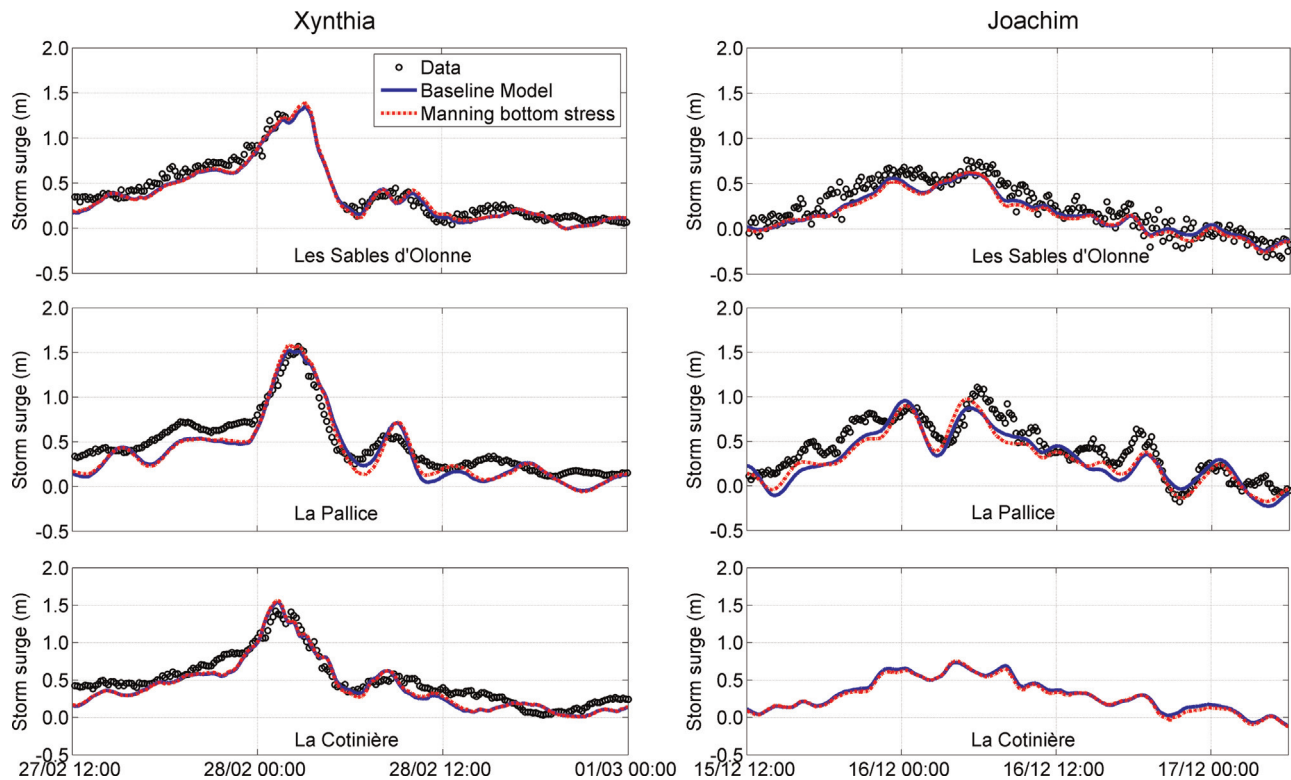


Fig. 15. Observed (black circles) against computed storm surges with a Manning parameterization bottom stress (red) and a wave-dependent parameterization (blue) at Sables d'Olonne, La Pallice and La Cotinière for storms Xynthia and Joachim. (For interpretation of the references to color in this figure legend, the reader is referred to the web version of this article.)

spatial resolution at high tide and second due to our 2DH approach, which prevents a proper representation of the vertical circulation that takes place in breaking zones. Our modeling system is currently being improved to integrate the latest developments on wave–current interactions in 3D (e.g. Bennis et al., 2011), which will allow investigating the importance of these phenomenon on storm surges.

Finally, the numerical experiments on a wave-dependent bottom stress were less convincing and did not allow drawing any particular conclusions. The little differences obtained between the various approaches suggest that the tide gauges used in this study, located in intermediate water depth, were not suitable to investigate this process that is dominant in shallower depths. Measurements will have to be carried out in shallower waters to better investigate the impact of wave-enhanced bottom stress on storm surges.

Acknowledgements

The developers of SELFE are greatly acknowledged. Water level data used in this study originate from the portal REFMAR (<http://refmar.shom.fr/>). Tidal boundary conditions were provided by Florent Lyard from UMR 5566 LEGOS. Wave data Offshore Oléron Island were provided by the French Oceanographic and Hydrographic Institute (SHOM) and these data were acquired in the scope of the projects MOUTON (funded by DGA PEA 012401) and EPIGRAM (funded by LEFE/IDAO and ANR, agreement ANR-08-BLAN-0330-01). Wave data in the Bay of Biscay were provided by Météo France, CETMEF and Puerto del Estado. The development of SELFE regarding wave–current interactions was performed in the context of the project DYNAMO, funded by the French National Research Agency (Grant agreement no. ANR-12-JS02-00008-01). Finally, Aron Roland benefited from an invited researcher grant from Region Poitou-Charente during his visit to La Rochelle.

References

- Abgrall, R., 2006. Residual distribution schemes: current status and future trends. *Comput. Fluids* 35 (7), 641–669. <http://dx.doi.org/10.1016/j.compfluid.2005.01.007>.
- André, C., Monfort, D., Bouzit, M., Vinchon, C., 2013. Contribution of insurance data to cost assessment of coastal flood damage to residential buildings: insights gained from Johanna (2008) and Xynthia (2010) storm events. *Nat. Hazards Earth Syst. Sci.* 13, 2003–2012. <http://dx.doi.org/10.5194/nhess-13-2003-2013>.
- Aptosos, A., Raubenheimer, B., Elgar, S., Guza, R.T., Smith, J.A., 2007. Effects of wave rollers and bottom stress on wave setup. *J. Geophys. Res.* 112, C02003. <http://dx.doi.org/10.1029/2006JC003549>.
- Ardhuin, F., Rogers, E., Babanin, A.V., Filipot, J.-F., Magne, R., Roland, A., van der Westhuysen, A., Queffelec, P., Lefevre, J.-M., Aouf, L., Collard, F., 2010. Semi-empirical dissipation source functions for ocean waves. Part I: definition, calibration, and validation. *J. Phys. Oceanogr.* 40, 1917–1941.
- Azevedo, A., Oliveira, A., Fortunato, A.B., Zhang, Y., Baptista, A.M., 2014. A cross-scale numerical modeling system for management support of oil spill accidents. *Mar. Pollut. Bull.* 80 (1–2), 132–147 (Original Research Article).
- Battjes, J.A., Janssen, J., 1978. Energy loss and set-up due to breaking of random waves. In: Paper presented at 16th International Conference on Coastal Engineering, Coastal Engineering Research Council, Hamburg, Germany.
- Bennis, A.C., Ardhuin, F., Dumas, F., 2011. On the coupling of wave and three dimensional circulation models: choice of theoretical framework, practical implementation and adiabatic tests. *Ocean Model.* 3–4, 260–272.
- Bennis, A.C., Dumas, F., Ardhuin, F., Blanche, B., 2014. Mixing parameterization: impacts on rip currents and wave set-up. *Ocean Eng.* 84, 213–227.
- Bertin, X., Li, K., Roland, A., Breilh, J.F., Zhang, Y.L., Chaumillon, E., 2014. A modeling-based analysis of the flooding associated with Xynthia, central Bay of Biscay. *Coast. Eng.* 94, 80–89.
- Bertin, X., Chaumillon, E., Sottolichio, A., Pedreros, R., 2005. Tidal inlet response to sediment infilling of the associated bay and possible implications of human activities: the Marennes–Oléron Bay and Maumusson Inlet, France. *Cont. Shelf Res.* 25, 115–1131.
- Bertin, X., Castelle, B., Chaumillon, E., Butel, R., Quique, R., 2008. Longshore transport estimation and inter-annual variability at a high energy dissipative beach: Saint Trojan beach, SW Oléron Island, France. *Cont. Shelf Res.* 28, 1316–1332.
- Bertin, X., Fortunato, A.B., Oliveira, A., 2009. A modeling-based analysis of processes driving wave-dominated inlets. *Cont. Shelf Res.* 29, 819–834.
- Bertin, X., Bruneau, N., Breilh, J.F., Fortunato, A.B., Karpytchev, M., 2012. Importance of wave age and resonance in storm surges: the case Xynthia, Bay of Biscay. *Ocean Model.* 42, 16–30.
- Bertin, X., Prouteau, E., Letetrel, C., 2013. A significant increase in wave height in the North Atlantic Ocean over the 20th century. *Glob. Planet. Change* 106, 77–83.

- Breilh, J.-F., Chaumillon, E., Bertin, X., Gravelle, M., 2013. Assessment of static flood modeling techniques: application to contrasting marshes flooded during Xynthia (western France). *Nat. Hazards Earth Syst. Sci.* 13, 1595–1612. <http://dx.doi.org/10.5194/nhess-13-1595-2013>.
- Bidlot, J.-R., Li, J.-G., Wittmann, P., Faucher, M., Chen, H., Lefevre, J.-M., Bruns, T., Greenslade, D., Arduhin, F., Kohno, N., Park, S., Gomez, M., 2007a. Inter-comparison of operational wave forecasting systems. In: Proceedings of 10th International Workshop on Wave Hindcasting and Forecasting and Coastal Hazard Symposium, North Shore, Oahu, Hawaii, November 11–16.
- Bidlot, J.-R., Janssen, P., Abdalla, S., 2007b. A revised formulation of ocean wave dissipation and its model impact. ECMWF Technical Memorandum 509, ECMWF, Reading, United Kingdom, 27 pp. Available online at <http://www.ecmwf.int/publications/>.
- Bidlot, J.-R., 2012. Present status of wave forecasting at ECMWF. In: Proceedings from the ECMWF Workshop on Ocean Waves. ECMWF, Reading, United Kingdom, 25–27 June 2012.
- Blake, E.S., 2007. The deadliest, costliest and most intense United States tropical cyclones from 1851 to 2006 (and other frequently requested hurricane facts). NOAA Technical Memorandum NWS TPC. 5, 43 pp.
- Brown, J.M., Wolf, J., 2009. Coupled wave and surge modelling for the eastern Irish Sea and implications for model wind-stress. *Cont. Shelf Res.* 29 (10), 1329–1342.
- Bowen, A.J., Inman, D.L., Simmons, V., 1968. Wave “set-down” and wave “set-up”. *J. Geophys. Res.* 73, 2569–2577.
- Charnock, H., 1955. Wind stress on a water surface. *Q. J. R. Meteorol. Soc.* 81, 639–640.
- Chaumillon, E., Proust, J.-N., Menier, D., Weber, N., 2008. Incised valley morphologies and sedimentary-fills within the inner shelf of the Bay of Biscay (France): a synthesis. *J. Mar. Syst.* 72, 383–396.
- Dietrich, J.C., Bunya, S., Westerink, J.J., Ebersole, B.A., Smith, J.M., Atkinson, J.H., et al., 2010. A high resolution coupled riverine flow, tide, wind, wind wave and storm surge model for southern Louisiana and Mississippi: Part II – synoptic description and analyses of Hurricanes Katrina and Rita. *Mon. Weather Rev.* 138, 378–404.
- Dodet, G., Bertin, X., Taborda, R., 2010. Wave climate variability in the North-East Atlantic Ocean over the last six decades. *Ocean Model.* 31 (3–4), 120–131.
- Dodet, G., Bertin, X., Bruneau, N., Fortunato, A.B., Nahon, A., Roland, A., 2013. Wave-current interactions in a wave-dominated tidal inlet. *J. Geophys. Res. Oceans* 118, 1587–1605. <http://dx.doi.org/10.1002/jgrc.20146>.
- Donelan, M.A., Dobsen, F., Smith, S., Anderson, R., 1993. On the dependence of sea surface roughness on wave development. *J. Phys. Oceanogr.* 23, 2143–2149.
- Doodson, A.T., 1924. Meteorological perturbations of sea-level and tides. *Geophys. J. Int.* 1, 124–147.
- Eldeberky, Y., 1996. Nonlinear Transformations of Wave Spectra in the Nearshore Zone (Ph.D. thesis of Delft University of Technology). The Netherlands, Delft, p. 203.
- Flather, R.A., 2001. Storm surges. In: Steele, J., Thorpe, S., Turekian, K. (Eds.), *Encyclopedia of Ocean Sciences*. Academic, San Diego, California, pp. 2882–2892.
- Grant, W.D., Madsen, O.S., 1979. Combined wave and current interaction with a rough bottom. *J. Geophys. Res.* 84 (C4), 1797–1808. <http://dx.doi.org/10.1029/JC084iC04p01797>.
- Hasselmann, S., Hasselmann, K., Allender, J.H., Barnett, T.P., 1985. Computations and parameterizations of the linear energy transfer in a gravity wave spectrum, II, parameterizations of the nonlinear transfer for application in wave models. *J. Phys. Oceanogr.* 15, 1378–1391.
- Hasselmann, K., Barnett, T.P., Bouws, E., Carlson, D.E., Hasselmann, P., 1973. Measurements of wind-wave growth and swell decay during the Joint North Sea Wave Project (JONSWAP). *Deutsch. Hydrogr. Z.* 8 (12), 95–102.
- Holthuijsen, L.H., Powell, M.D., Pietrzak, J.D., 2012. Wind and waves in extreme hurricanes. *J. Geophys. Res.* 117, C09003.
- Idier, D., Dumas, F., Muller, H., 2012. Tide-surge interaction in the English Channel. *Nat. Hazards Earth Syst. Sci.* 12, 3709–3718.
- Janssen, P.A.E.M., 1989. Wave-induced stress and the drag of air flow over sea waves. *J. Phys. Oceanogr.* 19, 745–754.
- Janssen, P.A.E.M., 1991. Quasi-linear theory of wind wave generation applied to wave forecasting. *J. Phys. Oceanogr.* 21, 1631–1642.
- Janssen, P.A.E.M., Saetra, O., Wetters, C., Hersbach, H., 2004. Impact of the sea state on the atmosphere and ocean. *Ann. Hydrogr.* 6e série, 3 (772), 2004.
- Janssen, P.A.E.M., Breivik, O., Mogensen, K., Vitart, F., Balmaseda, M., Bidlot, J.-R., Keeley, S., Leutbecher, M., Magnusson, L., Molteni, F., 2013. Air–sea interaction and surface waves, ECMWF, Technical Memorandum. 712, 34 pp.
- Jelesnianski, C.P., 1965. Numerical calculation of storm tides induced by a tropical storm impinging on a continental shelf. *Mon. Weather Rev.* 93, 343–358.
- Jones, J.E., Davies, A.M., 1998. Storm surge computations for the Irish Sea using a three-dimensional numerical model including wave–current interaction. *Cont. Shelf Res.* 18, 201–251.
- Kennedy, A.B., Westerink, J.J., Smith, J.M., Hope, M.E., Hartman, M., Taflanidis, A.A., Tanaka, S., Westerink, H., Cheung, K.F., Smith, T., Hamann, M., Minamide, M., Ota, A., Dawson, C., 2012. Tropical cyclone inundation potential on the Hawaiian Islands of Oahu and Kauai. *Ocean Model.* 52–53, 54–68. <http://dx.doi.org/10.1016/j.ocemod.2012.04.009>.
- Le Cann, B., 1990. Barotropic tidal dynamics of the Bay of Biscay shelf: observations, numerical modelling and physical interpretation. *Cont. Shelf Res.* 10 (8), 723–758.
- Leonard, B.P., 1991. The ULTIMATE conservative difference scheme applied to unsteady one-dimensional advection. *J. Comput. Methods Appl. Mech. Eng.* 88, 17–74.
- Longuet-Higgins, M.S., Stewart, R.W., 1964. Radiation stress in water waves; a physical discussion with applications. *Deep-Sea Res.* 11, 529–562.
- Mastenbroek, C., Burgers, G., Janssen, P.A.E.M., 1993. The dynamical coupling of a wave model and a storm surge model through the Atmospheric Boundary Layer. *J. Phys. Oceanogr.* 23, 1856–1866.
- Miles, J.W., 1957. On the generation of surface waves by shear flows. *J. Fluid Mech.* 3, 185–204.
- Nicolle, A., Karpytchev, M., Benoit, M., 2009. Amplification of the storm surges in shallow waters of the Pertuis Charentais (Bay of Biscay, France). *Ocean Dyn.* 59, 821–935. <http://dx.doi.org/10.1007/s10236-009-0219-0>.
- Nicholls, R.J., Wong, P.P., Burkett, V.R., Codignotto, J.O., Hay, J.E., McLean, R.F., Ragoonaden, S., Woodroffe, C.D., 2007. Coastal systems and low-lying areas. *Climate change 2007: impacts, adaptation and vulnerability*. In: Change, M.L., Parry, O.F., Canziani, J.P., Palutikof, P.J., van der Linden, Hanson, C.E. (Eds.), *Contribution of Working Group II to the Fourth Assessment Report of the Intergovernmental Panel on Climate*. Cambridge University Press, Cambridge, UK, pp. 315–356.
- Olabarrieta, M., Warner, J.C., Armstrong, B., Zambon, J.B., He, R., 2012. Ocean–atmosphere dynamics during Hurricane Ida and Nor’Ida: an application of the coupled ocean–atmosphere–wave–sediment transport (COAWST) modeling system. *Ocean Model.* 43–44, 112–137.
- Pairaud, I.L., Lyard, F., Auclair, F., Letellier, T., Marsaleix, P., 2008. Dynamics of the semi-diurnal and quarter-diurnal internal tides in the Bay of Biscay. Part 1: Barotropic tides. *Cont. shelf Res.* 28, 1294–1315. <http://dx.doi.org/10.1016/j.csr.2008.03.004>.
- Pawluczak, R., Beardsley, B., Lentz, S., 2002. Classical tidal harmonic analysis including error estimates in MATLAB using T_TIDE. *Comput. Geosci.* 28, 929–937.
- Phillips, O.M., 1957. On the generation of waves by turbulent wind. *J. Fluid Mech.* 2, 417–445.
- Pinto, L., Fortunato, A.B., Zhang, Y., Oliveira, A., Sancho, F.E.P., 2012. Development and validation of a three-dimensional morphodynamic modelling system for non-cohesive sediments. *Ocean Model.* 57–58, 1–14.
- Pond, S., Pickard, G.L., 1998. *Introductory Dynamical Oceanography*. Butterworth-Heinemann.
- Powell, M.D., Vickery, P.J., Reinhold, T.A., 2003. Reduced drag coefficient for high wind speeds in tropical cyclones. *Nature* 422, 279–283.
- Proudman, J., 1957. Oscillations of tides and surge in an estuary of finite length. *J. Fluid Mech.* 2, 371–382.
- Rego, J.L., Li, C., 2010. Nonlinear terms in storm surge predictions: effect of tide and shelf geometry with case study from Hurricane Rita. *J. Geophys. Res.* 115, C06020.
- Rivière, C., Arbogast, P., Lapeyre, G., Maynard, K., 2012. A potential vorticity perspective on the motion of a mid-latitude winter storm. *Geophys. Res. Lett.* 39 (12), L12808.
- Rodrigues, M., Oliveira, A., Guerreiro, M., Fortunato, A.B., Menaia, J., David, L.M., Cravo, A., 2011. Modeling fecal contamination in the Aljezur coastal stream (Portugal). *Ocean Dyn.* 61 (6), 841–856.
- Roland, A., Zhang, Y., Wang, H.V., Meng, Y., Teng, Y.C., Maderich, V., Brovchenko, I., Dutour-Sikirić, M., Zanke, U., 2012. A fully coupled 3D wave–current interaction model on unstructured grids. *J. Geophys. Res.* 117. <http://dx.doi.org/10.1029/2012JC007952>.
- Sheng, Y.P., Zhang, Y., Paramygin, V.A., 2010. Simulation of storm surge, wave, and coastal inundation in the Northeastern Gulf of Mexico region during Hurricane Ivan in 2004. *Ocean Model.* 35 (4), 314–331.
- Smith, S.D., Banke, E.G., 1975. Variation of the sea surface drag coefficient with wind speed. *Q. J. R. Meteorol. Soc.* 101, 665–673.
- Smith, K., 1996. *Environmental Hazards: Assessing Risk and Reducing Disaster*, 2nd ed. Routledge, London.
- Soulsby, R., 1997. *Dynamics of Marine Sands, a Manual for Practical Applications*. Thomas Telford, H.R. Wallingford, England, ISBN: 0-7277-2584X.
- Stewart, R.W., 1974. The air–sea momentum exchange. *Bound. Layer Meteorol.* 6, 151–167.
- Swart, D.H., 1974. *Offshore Sediment Transport and Equilibrium Beach Profiles*. Delft Hydraulics Lab Publication, Delft, The Netherlands, p. 131.
- Takagaki, N., Komori, S., Suzuki, N., Iwano, K., Kuramoto, T., Shimada, S., Kurose, R., Takahashi, K., 2012. Strong correlation between the drag coefficient and the shape of the wind sea spectrum over a broad range of wind. *Geophys. Res. Lett.* 39, L23604.
- Tolman, H.L., 2009. *User Manual and System Documentation of WAVEWATCH III version 3.14*. NOAA/NWS/NCEP/MMAB Technical Note 276, 194 p.
- Xie, L., Pietrafesa, L.J., Wu, K., 2003. A numerical study of wave–current interaction through surface and bottom stresses: coastal ocean response to hurricane Fran of 1996. *J. Geophys. Res.* 108 (C2), 3049–3066.
- Yanenko, N.N., 1971. *The Method of Fractional Steps*. Springer, Berlin <http://dx.doi.org/10.1007/978-3-642-65108-3>.
- Zhang, Y., Witter, R.W., Priest, G.P., 2011. Nonlinear tsunami–tide interaction in 964 Prince William Sound tsunami. *Ocean Model.* 40 (3–4), 246–259.
- Zhang, Y.L., Baptista, A.M., 2008a. SELFE: a semi-implicit Eulerian–Lagrangian finite-element model for cross-scale ocean circulation. *Ocean Model.* 21 (3–4), 71–96.
- Zhang, Z., Xiao, C., Shen, J., 2008b. Comparison of the CEST and SLOSH models for storm surge flooding. *J. Coast. Res.* 24 (2), 489–499.